Acta Biomaterialia 48 (2017) 270–288

Contents lists available at ScienceDirect

Acta Biomaterialia

journal homepage: www.elsevier.com/locate/actabiomat

Full length article

# Seagull feather shaft: Correlation between structure and mechanical response

Bin Wang, Marc André Meyers *

*University of California, San Diego, La Jolla, CA 92093-0411, USA*

ARTICLE INFO

*Article history:*
Received 28 May 2016
Received in revised form 18 October 2016
Accepted 2 November 2016
Available online 3 November 2016

*Keywords:*
Feather shaft
Hierarchical fibrous structure
Nanomechanical properties
Compression
Flexure

ABSTRACT

Flight feathers are unique among a variety of keratinous appendages in that they are lightweight, stiff and strong. They are designed to withstand aerodynamic forces, but their morphology and structure have been oversimplified and thus understudied historically. Here we present an investigation of the shaft from seagull primary feathers, elucidate the hierarchical fibrous and porous structure along the shaft length, and correlate the tensile and nanomechanical properties to the fiber orientation. An analysis of the compressive behavior of the rachis based on a square-section model shows a good fit with experimental results, and demonstrates the synergy between the cortex and medulla. Flexural properties of the shaft along the shaft length, analyzed as a sandwich composite, reveal that although all flexural parameters decrease towards the distal shaft, the specific equivalent flexural modulus and strength increase by factors of 2 and 3, respectively. The failure mode in flexure for all specimens is buckling on the compressive surface, whereas the foamy medulla prevents destructive axial cracking and introduces important toughening mechanisms: crack deflection, fiber bridging, and microcracking.

**Statement of Significance**

Using mechanics principles, we analyze the feather shaft as a composite beam and demonstrate that the flexural strength is extraordinary, considering its weight and tailored along the length. The cross section changes from circular in the proximal base to square/rectangular in the distal end. We also discovered that the composite design, a solid shell enclosing a foam core, produces synergistic strengthening and toughening to the feather at a minimum of weight.



## 1. Introduction

Among a plethora of biological materials that may serve as a source of bioinspiration, feathers stand out with extraordinary mechanical properties that have evolved for flight: lightweight, stiff and strong, yet able to flex, which are coincidently the goals of many modern structural materials. Flight feathers primarily bend during flight, and have to sustain aerodynamic forces within allowable flexural/torsional strains. The central feather shaft provides major mechanical support, and consists of calamus (below the skin) and rachis (above the skin), shown in Fig. 1. It is composed of a solid keratinous shell, called cortex, enclosing a foamy core named medulla; the cortex contains the dorsal, lateral and ventral regions (specified in Fig. 1a).

The feather shaft exemplifies a naturally designed composite beam facilitating flight; it is of paramount importance to unravel the functionalities by correlating the structure with mechanical properties. It is entirely composed of β-keratin proteins [1–5], which generally show higher stiffness and strength than α-keratin based materials [6]. The shell (cortex) shows an ultra-fine filament-matrix structure at the nanoscale, ~3.5 nm β-keratin filaments [7] formed from β-pleated sheets. It displays a fibrous structure at microscale: axial fibers covered by thin superficial circumferential fibers [8–10] and crossed-fibers observed through selective degradation [11].

There have been plenty of studies [8,12–14] on the tensile response of cortex; however, the specific sampling locations usually were not specified. The broad range of reported Young's moduli of feather keratin from different species has been attributed to the experimental procedures [12]. However, it should be kept in mind that the anisotropy of feather cortex along the whole shaft

* Corresponding author.
*E-mail address:* mameyers@ucsd.edu (M.A. Meyers).

http://dx.doi.org/10.1016/j.actbio.2016.11.006
1742-7061/

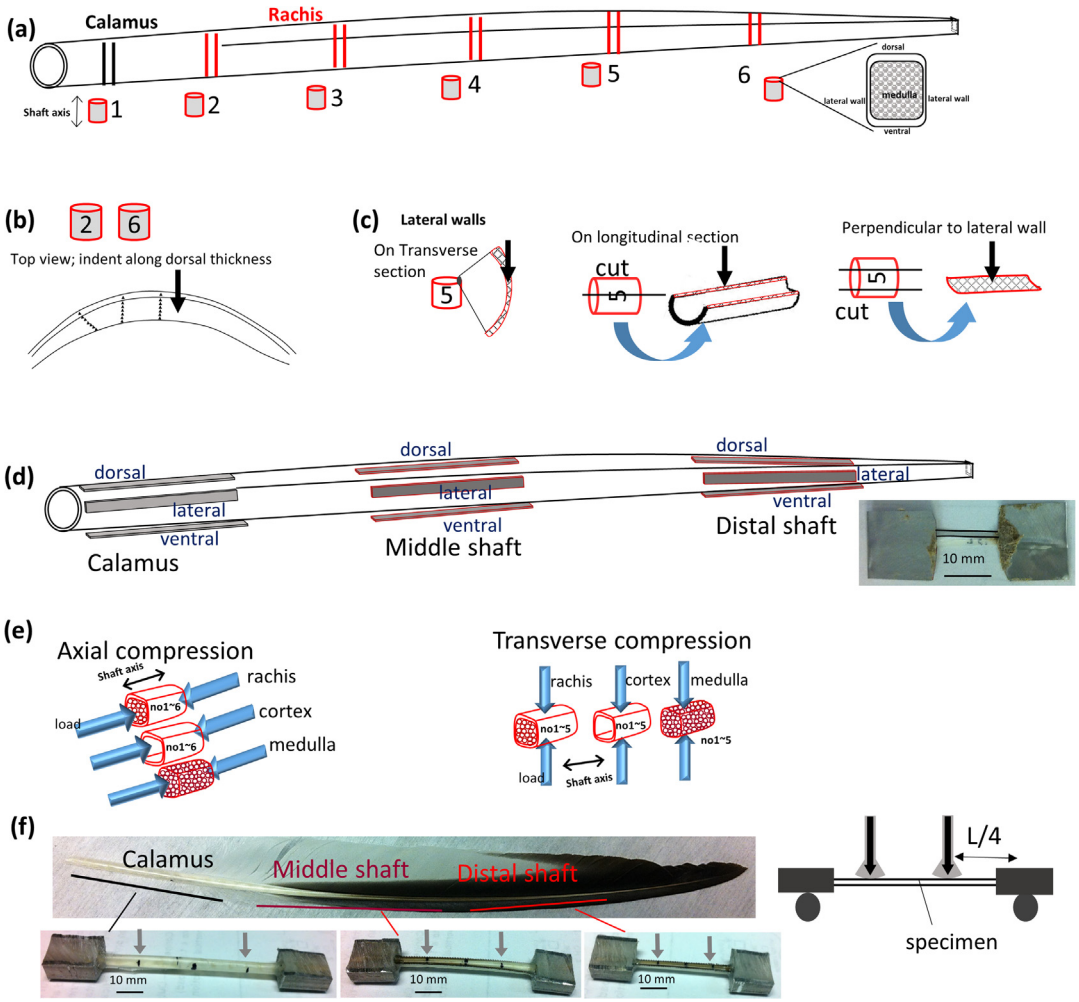


**Fig. 1.** (a) Specimens for structural observation: the feather shaft consists of calamus (proximal) and rachis, and is cut into cylindrical sections with numbers 1–6 representing positions along the shaft axis from the calamus to the distal end. Dorsal, lateral and ventral regions of cortex on transverse cross section are shown. Nanoindentation (b) on the dorsal region along cortex thickness at positions 2 and 6, and (c) in three loading orientations including on transverse section, longitudinal section and perpendicular to lateral wall at position 5. (d) Tensile tests on thin strips at dorsal, lateral and ventral regions at calamus, middle shaft and distal shaft, with a photo of specimen ready for test. (e) Axial and transverse compression specimens, both include rachis, cortex and medulla. (f) Four-point flexure along the shaft length including calamus, middle shaft and distal shaft; the two ends of each specimen were embedded in epoxy and square tubes, and the loading points are indicated by arrows.

length and among cortical regions at a given location also contribute to the discrepancy.

Widely present in nature, sandwich structures save weight and increase the buckling resistance during compression. Theoretical analyses on foam-filled cylindrical shells have been developed [15–18]. The feather rachis is distinguished from other biological shell-over-foam materials in that it possesses a square cross section. However, studies on the compressive behavior of the feather shaft have been very rare, and only on flightless feathers via simple cylinder models [13,19]. No attempts have been made to incorporate the square cross section into a quantitative analysis of the buckling of feather rachis, which, nevertheless, presents the real scenario for most flight feather rachises. Additionally, our understanding of the function of the foam core (medulla) is quite limited due to the few and somewhat controversial reported studies: medulla removal has no significant effect on buckling stress or tensile strength [1]; medulla removal leads to 16% more flexural deflection [2]; in vivo strain measurement in pigeons suggests buckling to be the most important mode of failure [3]; the peacock's tail feather rachis splits before buckling [4]. A comprehensive and rigorous examination of the compressive behavior of flight feather rachis is therefore needed.

The feather shaft bends both naturally (all feathers) and under aerodynamic forces (flight feathers). A few reports describe the response of the feather rachis in cantilever beam bending [13,20–23], three-point bending [24] and four-point bending [25] at very small deformation (elastic region) and neglect the cellular medulla. Although the medulla does play a role in the feather performance [20,24], its effect and function in bending behavior have not been investigated considering the rachis as a composite.

In an aim to address the above issues, this work provides a thorough and rigorous study of the biomechanics of the seagull feather shaft with quantitative analysis, correlating to the features involving the composite design and the hierarchical structure. Our findings and analysis are intended at stimulating the design of novel synthetic structures that can reproduce the remarkable properties of the feather shaft.

## 2. Materials and experimental procedures

### 2.1. Materials

Primary flight feathers from two juvenile California gulls (*Larus californicus*) were collected, after the natural death of the birds,

under the Federal Fish and Wildlife Permit; the shafts were used for structural analysis and mechanical testing. The feathers were stored and studied at room temperature and humidity. Primary feathers from other seagulls were also studied, and the results are shown in Supplementary Material III.

### 2.2. Structural characterization

For optical microscopic observation, the feather shafts were cut into six segments along the shaft axis (numbered as 1, 2, 3, 4, 5 and 6) from the proximal to the distal end (Fig. 1a). All segments were embedded in epoxy with transverse sections exposed, and polished using a series of graded sand papers up to 2400# and finally polishing paste (0.3 μm aluminum oxides). For scanning electron microscopy (SEM), transverse and longitudinal sections of feather shaft segments were obtained by cutting and folding or breaking at different positions along the shaft length, and coated with iridium for observation. The lateral walls of feather rachis cortex were submerged in liquid nitrogen, fractured in longitudinal direction and also coated with iridium. Axio Fluorescence and Phillips XL30 environmental scanning electron microscopes at the Nano3 facility at Calit2, UCSD, were used.

For transmission electron microscopy (TEM), TGA-$OsO_4$ staining [26] combined with post-staining by lead was used. Pieces of ventral cortex (approximately 3 mm × 2 mm) from seagull feather rachis were pre-treated by immersing in 0.5 M thioglycolic acid (pH 5.5) for 24 h at room temperature to enhance the contrast between the filaments and matrix. Then the pieces were washed with double-distilled water for 1 h and immersed in 1–2% aqueous osmium tetroxide ($OsO_4$) for 3 days at room temperature. The stained pieces were washed with distilled water, dehydrated to 100% ethanol through a series of graded alcohol solutions and then transited to 100% acetone through graded mixtures of ethanol and acetone. The specimens were subsequently infiltrated using Spurr's low viscosity epoxy resin through a series of solutions with increasing amounts of resin and decreasing amounts of acetone (25% resin + 75% acetone, 50% resin + 50% acetone, 75% resin + 25% acetone, 90% resin + 10% acetone, 100% resin, 100% resin), each taking one day. Specimens were then placed in fresh resin and polymerized with appropriate orientation for 2 days at 65 °C. The embedded specimens were trimmed and sectioned using a Leica Ultracut UCT ultramicrotome using a diamond blade. Silver sections were picked up on filmed grids, post-stained with lead for 60 s, and further coated with graphite. An FEI Technai 12 (Spirit) (120 kV) transmission electron microscope was used for examination.

### 2.3. Mechanical properties

The water content of natural feathers is typically lower than 10 wt% [27,28], which conforms to the ambient-dried feathers [19]. Thus, specimens from seagull feather shafts for mechanical studies were tested in ambient condition.

#### 2.3.1. Nanoindentation testing

The feather shaft was numbered and cut into similar segments to the ones for structural evaluation (Fig. 1a). Three types of specimens were prepared and polished using graded sand papers and 0.3 μm polishing paste: (I) cortex segments were mounted in epoxy with transverse sections polished; (II) cortex segments were further cut along the shaft axis so that longitudinal sections were exposed and polished; (III) cortex segments at certain positions were cut into dorsal and lateral pieces and the external surfaces were polished. Two groups of experiments were performed: (1) mechanical variation along dorsal cortex thickness, at positions #2 and #6, via indenting on transverse sections from inner to outer regions (Fig. 1b); (2) mechanical variation among different orientations, via indenting on lateral wall at position #5 from Type I, II and III specimens (Fig. 1c).

All specimens were placed in a fume hood for 2 days to attain ambient conditions before testing. The specimens were fixed on a steel block using Super Glue and the glue layer was sufficiently thin to have minimal impact on material testing. A nanoindentation testing machine (Nano Hardness Tester, Nanovea, CA, USA) and a Berkovich diamond tip (Poisson's ratio of 0.07 and elastic modulus of 1140 GPa) were used. All specimens were indented with 20 mN of maximum force, at loading and unloading rates of 40 mN/min, and 20 s of creep.

The hardness and reduced Young's moduli were calculated from the load-displacement curves according to ASTM E2546 and the Oliver Pharr method [29,30], which is installed in the Nanovea tester (see Supplemental Material I). A value of 0.3 for Poisson's ratio of feather keratin was used according to the reported values of keratinous materials in the literature (0.25 for sheep horn [31]; 0.3 for fingernails [32]; 0.37–0.48 for hair keratin [33]). An average of five consistent measurements for each position was reported.

#### 2.3.2. Tensile testing

The variation of dorsal, ventral and lateral cortex along the shaft length was examined. Feather shafts were divided into three segments along the shaft length (calamus, middle shaft and distal shaft). Then, dorsal, lateral, and ventral cortex pieces along the shaft axis of each segment were excised (the medullary core was carefully removed to avoid scratches) to obtain thin rectangular strips (Fig. 1d). The termini of each rectangular strip were fixed with LOCTITE glue between two sand paper sheets, leaving a test gauge length of 10 ± 1.05 mm. Fig. 1d shows one tensile specimen ready for testing. The width was 2.00 ± 0.21 mm, and the thickness varied from 0.10 mm to 0.29 mm. An Instron 3342 equipped with 500 N load cell was used, and all specimens were loaded in the direction of feather shaft axis at room temperature at a strain rate of $10^{-3}$/s.

#### 2.3.3. Compression testing

Specimens for two types of tests were prepared. For axial compression, rachises of Primary#3-left (flight feather numbered 3 on the left wing) and Primary#5-left (flight feather numbered 5 on the left wing) were cut consecutively into twelve sections (six sections for each rachis). The medulla of every other section was removed to obtain cortex specimens so that each rachis specimen follows cortex specimen along the rachis length: ax-rachis-no. 1, ax-cortex-no. 1, ax-rachis-no. 2, ax-cortex-no. 2, etc. (Fig. 1e). All are in near rectangular prism shape, about 3 × 3 × 4.5 $mm^3$ in size. Another rachis (Primary#4-left) was cut into consecutive sections and the exterior cortex was removed (by firstly cut longitudinally out the dorsal, ventral and lateral walls, and then trim very softly the shape of the medulla). Then all specimens were inspected for intactness and shape under microscope and unqualified ones, e.g. damaged cells, were discarded. Finally five foamy medullary specimens in near rectangular prism shape were obtained: ax-medulla-no. 1 to ax-medulla-no. 5, about 2 × 2 × 2 $mm^3$ in size.

For transverse compression, symmetrical feathers and the same sample preparation was used, except that the loading is dorsal-ventrally transverse (Fig. 1e). Rachises of Primary#3-right (flight feather numbered 3 on the right wing) and Primary#5-right (flight feather numbered 5 on the right wing) feathers were cut into twelve consecutive sections with the medulla of every other section removed. Medullary specimens were obtained from Primary#4-right feather rachis. Rachis, cortex (tr-rachis-no. 1, tr-cortex-no. 1, tr-rachis-no. 2, tr-cortex-no. 2, etc.) and medulla (tr-medulla-no. 1 to tr-medulla-no. 5) specimens in transverse loading are shown in Fig. 1e. Cross sectional areas of all specimens

were determined by using Image J calculations on optical micrographs of the specimens. All tests were conducted in ambient environment at a strain rate of $10^{-3}$/s.

*2.3.4. Four-point flexure testing*

Whole primary flight feather shafts (Primary#1-#3) were divided into three segments along the shaft length: calamus, middle shaft and distal shaft. The shaft segments were loaded in four-point bending with the distance of loading application points being one half of the support span, shown in Fig. 1f (loading points indicated by arrows). This flexure configuration was chosen since it creates a uniform moment between the loading points, and provides a more accurate examination of the flexural behavior along the shaft length. Cantilever beam bending was avoided because of somewhat inaccurate measurements of flexural deflection (due to the longitudinal curvature of the shaft and large displacement) and it is more suitable for determining elastic behavior than failure mode. Three-point bending was not adopted because it produces significant local stress concentration at the load point, which is not the usual case for flight feathers, and underestimates the failure stress.

The two ends of each whole shaft segment were embedded in epoxy in short, thin and square aluminum tubes to prevent their twisting during testing. Loads were applied on the shaft segments and care was taken to prevent compressing tubes and assure free rotation of the ends. Rubber pads on loading points and supporting bars were used to prevent local concentrated damage. The dorsal surfaces of specimens were loaded until the load dropped, which simulates fairly closely the real stress condition of flight feathers [25]. Specimens ready for testing are shown in Fig. 1f. All shaft specimens have a ratio of support length over specimen depth (at middle point) of 16:1, following the ASTM D6272, and the loading rate was 0.01 mm/s at room temperature for all specimens.

*2.3.5. Statistical methods*

All experimental measurements were analyzed by standard deviation through Excel. For nanoindentation and compression, each data point represents the average of five consistent measurements, and the error bars/errors represent standard deviations. In tensile testing, stress-strain curves of all cortical specimens along the shaft length were plotted and grouped in different colors; the Young's modulus, tensile strength and breaking strain represent averages of four valid test results, and the error bars represent standard deviations. For four-point bending, flexural rigidity, area moment of inertia, flexural modulus and flexural strength of shaft segments along the shaft length were averages of three valid experiments, respectively, and the errors represent standard deviations.

## 3. Structure

### 3.1. Cross-sectional shape change of the cortex

A distinct feature of the seagull feather shaft is the shape variation along the shaft length, as compared with non-flight feathers, shown in Fig. 2. From the calamus to the rachis, images of transverse sections show that the cortex changes shape from circular to rectangular. In addition, towards the distal rachis, the dorsal and ventral regions of cortex are much thicker than the lateral walls. The cross sectional shape change of cortex is instrumental in increasing the flexural rigidity (the product of the longitudinal modulus, $E$, and the dorsalventral area moment of inertia, $I$) along the shaft axis [34]. Feather shafts from other volant birds generally show such a shape factor gradient, e.g. pigeon [20], bar owl [23], seriema, and crow [34].

However, for the wing feather shaft from an ostrich (flightless bird), the cortex shows uniformly circular/elliptical shape decreasing in size throughout the shaft length; the shape changes to near triangular only at the end. Similarly, the peacock tail feather shaft (flightless feather from flying bird) shows generally circular cross sections along the shaft length; the shape changes to near pentagonal shape at the very distal end. The uniform circular cortex of peacock tail feather shaft was also reported [13,19]. Additionally, the thicknesses of dorsal, lateral and ventral regions of cortices of both flightless feather shafts are approximately constant along the shaft length (~235 μm for ostrich wing feather and ~111 μm for peacock tail feather).

Hollow beams with square cross sections have flexural advantages over circular ones in providing higher flexural rigidity per unit area and superior ability in resisting cross sectional shape change, whereas circular tubes having the same sectional area start and continue ovalization, losing the ability to sustain further load [34]. The cortex of rachis resembles an I-beam that distributes material to maximize the area moment of inertia to resist flexural deformation, while the flightless feather shaft has a uniformly thick cortex. Therefore, the shape factor of cortex subtly compensates for the decreasing area moment of inertia towards the distal rachis caused by the significant decrease of mass to reduce profile drag. Thus, the desired flexural rigidity is maintained [34]. On the other hand, flightless feathers are not demanded to sustain the complex forces and flexural strains generated by flight, and therefore do not need to involve sophisticated shape changes.

Other structural features of the seagull feather shaft include a ventral groove (blue rectangle in Fig. 2a), which starts in the middle of ventral surface at proximal rachis (positions 2 and 3) and is present axially for the entire rachis. A transverse septum (indicated by pink dotted line) and foam-like medulla starts to develop from the ventral region; it gradually fills the cortex towards distal end. The proximal rachis has the thickest and largest cortex. The foam-filled rachis is approximately 70% of the shaft length for the seagull feather. Flightless feathers have a relatively longer rachis region, about 96% and 94% of total shaft length for peacock tail and ostrich wing feathers, respectively. They do not show a transverse septum within the medulla.

### 3.2. Layered fibrous structure of the cortex

The cortex shows a complex layered structure composed of differently oriented fibers along the shaft length (Fig. 3). At the calamus, the dorsal, lateral and ventral regions of cortex consist of a thin outer layer and a thick inner layer, seen from transverse sections in Fig. 3a. Longitudinal sections of these three cortical regions (Fig. 3b) reveal that the outer layer is composed of circumferential fibers while the thick inner layer consists of axial (longitudinal) fibers. At the proximal rachis (beginning rachis), transverse sections of cortex show that the dorsal region consists of a thinner outer layer and a thick inner layer, while only one layer is observed for both lateral and ventral regions. Longitudinal sections exhibit that outer circumferential fibers covering the inner axial fibers exist in the dorsal region, whereas the lateral walls are composed of crossed-lamellae and the ventral region of solely axial fibers (Fig. 3d). At the distal rachis, the entire cortex shows one uniform layer; dorsal and ventral regions are comprised of axial fibers, while the lateral walls crossed-lamellae. The crossed-lamellae, present along the entire rachis in the lateral walls, are indicative of crossed-fiber structure (Fig. 3f-lateral). The inner layer shows constituent fibrils/fibers ranging from ~64 nm to 2 μm diameter.

Transmission electron micrographs of the ventral region of rachis cortex reveal a hierarchical fibrous structure (Fig. 4): the rachis cortex is ~2 mm, and consists of keratinized cortical cells (keratinized cells are dead epidermal cells that compose keratinous

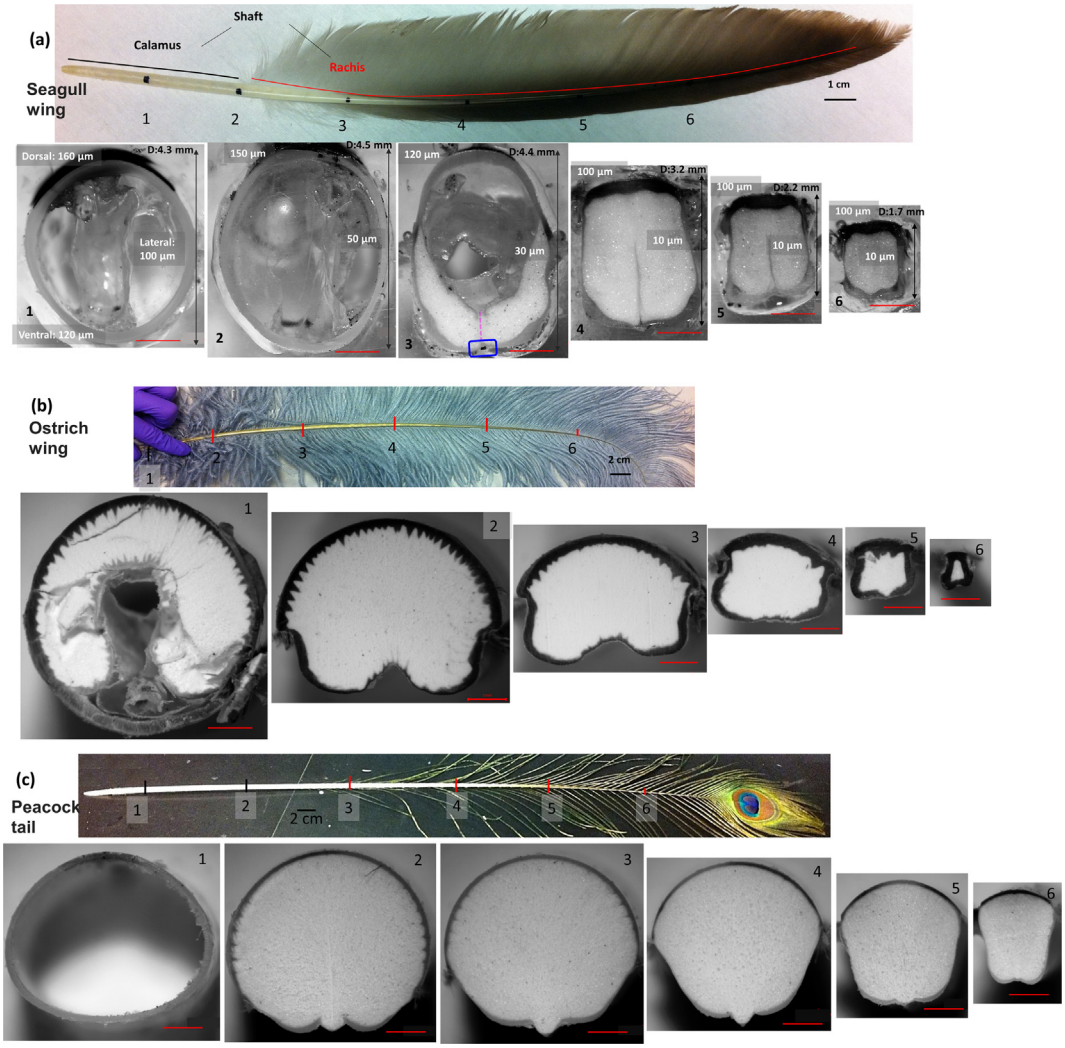


**Fig. 2.** Cross-sectional shape change along feather shafts: (a) seagull wing flight feather; numbered shaft represents the normalized distance from calamus to distal shaft and optical micrographs of the transverse sections along the shaft length; the thicknesses of dorsal, ventral and lateral cortex are indicated in white numbers, and the dorsal-ventral depth (D) of cortex in black numbers; (b) ostrich wing feather; numbered shaft and optical micrographs of the transverse sections showing the cortex shape; (c) peacock's tail feather; numbered shaft and optical micrographs of the transverse sections showing the cortex shape. Scale bars, 1 mm.

materials [6]). The cells are separated by a cell membrane complex, which shows a characteristic densely-stained central layer (δ) sandwiched between two less-dense layers (β), about 22–26 nm thick, similar to other keratinized materials, e.g. rat claw [2] and wool [35]. Inside the cells there are fibrils about 100–400 nm in diameter clearly outlined by the densely stained material (black peripheries). These are identified as macrofibrils, being at the same structural hierarchical level of macrofibrils in α-keratin, e.g. human hair. The remainder is intermacrofibrillar material. Within the macrofibrils, β-keratin filaments, or microfibrils, are the structural counterpart of the intermediate filaments in α-keratin, and have circular cross sections ~3 nm; they are delineated by the $OsO_4$ + -lead stained matrix. The filamentous nature and the structural hierarchy of feather keratin are similar to those of the α-keratin, while differences exist: (1) in α-keratin, microfibrils (intermediate filaments) show fairly distinct regions of well aligned or specialized patterns; but such well aligned arrangements of microfibrils (β-keratin filaments) are rare in feather keratin, meaning a higher degree of randomness in filamentous organization [7]. (2) The necessity to use post-lead staining for matrix indicates that the cystine content of the matrix is not so greatly different from that of microfibrils as α-keratin, though results are also suggestive of an amorphous matrix [7].

Scanning electron micrographs of tensile fractured rachis cortex strips confirm the hierarchy of structure: fibers measuring ~5 μm wide and sub-fibers (50–300 nm in diameter) (Fig. 4d and e). The latter are the macrofibrils observed from transmission electron micrographs. Taking into consideration that each lamella in the lateral walls (Fig. 3d and f) represents one layer of keratinized cells, the cortical cells can be estimated to be about ~2 μm thick and 30 μm wide. These cells contain macrofibrils (100–400 nm) surrounded by intermacrofibrillar material; the macrofibrils consist of β-keratin filaments (~3 nm) embedded an amorphous matrix.

### 3.3. Porous and fibrous structure of the medulla

The medulla, the cellular core inside feather rachis, is a closed-cell foamy structure that has hierarchical levels of porosity at the micro- and nano-scales. It exhibits near round cells with a diameter about 20–30 μm (Fig. 5a, micro-scale porosity). Higher magnification images reveal that the cell walls are composed of curved weaving fibrils (about 40–130 nm in diameter), while the spaces between fibrils result in porosity at the nanoscale level, which further decreases density. This hierarchy had been previously revealed by Chen et al. [36]. The cell walls are connected and strengthened by fibrous struts at junctions and interfaces of cell

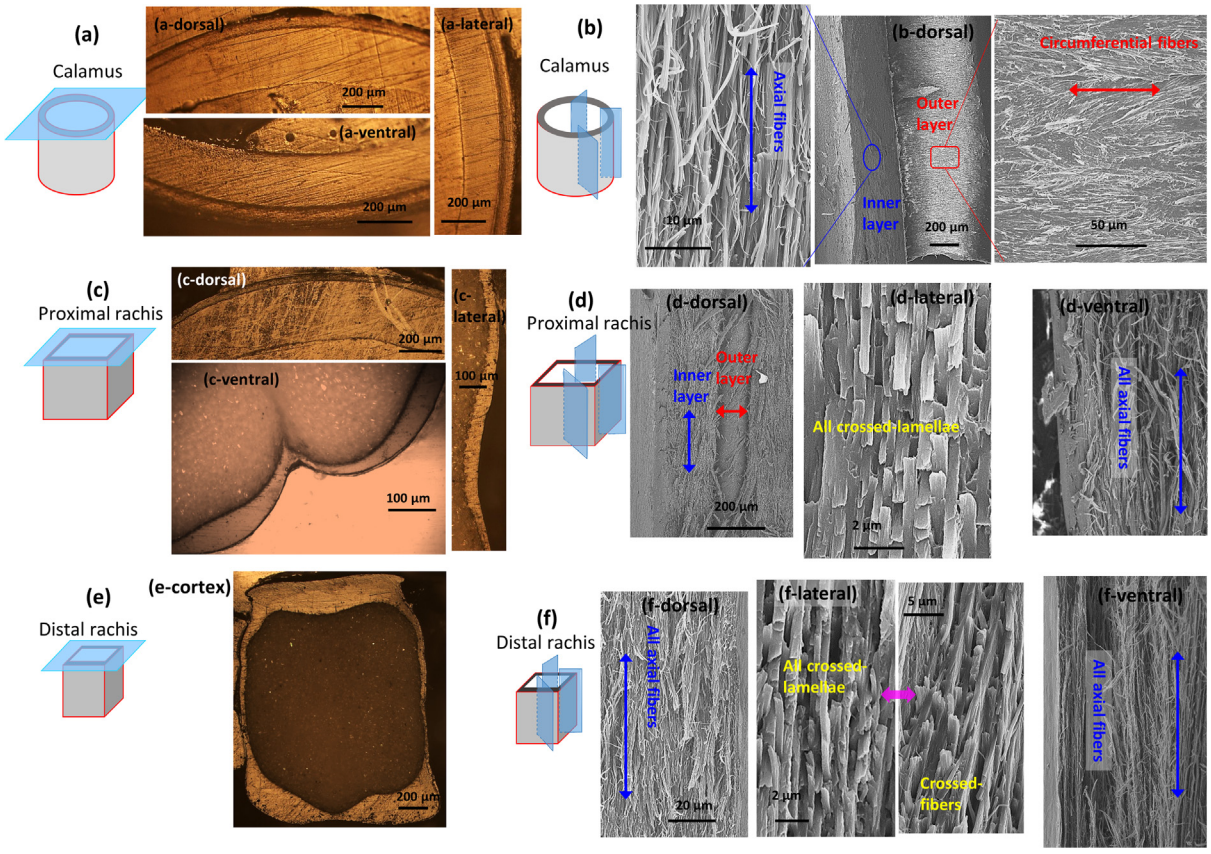


**Fig. 3.** The layered fibrous structure of cortex. At the calamus: (a) transverse sections of cortex in the dorsal, lateral and ventral regions, all show the two layered structure; (b) longitudinal sections of cortex in the dorsal region, representing dorsal, lateral and ventral regions, show that the outer circumferential fibers covers the inner axial fibers. At the proximal rachis: (c) transverse sections of cortex in the dorsal, lateral and ventral regions; (d) longitudinal sections of cortex in the dorsal region, lateral and ventral regions. At the distal rachis: (e) transverse section of the cortex; (f) longitudinal sections of cortex in the dorsal region, lateral and ventral regions. Blues planes represent the orientations of the corresponding optical/scanning electron micrographs and are perpendicular to the side surfaces of cortex. (For interpretation of the references to colour in this figure legend, the reader is referred to the web version of this article.)

walls (indicated by yellow rectangles in Fig. 5c and d). At the interface between cellular medulla and the cortex (Fig. 5e), the fibrils forming medullary cell walls merge with the fibrils comprising the cortex, thus forming a continuous structure.

The enhanced coherence within the medulla and the strong bonding between medulla and cortex contribute to the mechanical integrity and energy absorbance of the shaft. It is experimentally found that when cortex strips (dorsal, ventral and lateral walls) are loaded in axial tension, specimens with a thin layer of medulla exhibit a significant fracture delay and show a flat fracture surface compared with specimens without medulla, indicating that the medulla prevents the splitting of cortex. In addition, bending of shaft involves not only tension but also compression of the cortex and medulla. It has been documented, from a number of other similar biological materials, e.g. porcupine quills [37–39], plant stems [17,40], wood [38,41], that a porous core acts as an elastic foundation to increase the buckling resistance of the solid shell. We confirm here that the interface of shell and foamy core plays a vital role.

## 4. Mechanical response

### 4.1. Nanoindentation

From composite theory, the superior mechanical properties of the feather cortex are in the fiber axis direction [42,43]; therefore, nanoindentation of the feather cortex should generate different results according to the local fiber orientations. This is schematically shown in Fig. 6a and b. When the loading direction is parallel to the fibers, it puts them under compression and buckling is impeded by the matrix; loading perpendicular tends to separate fibers and the force is mostly endured by the softer matrix. Thus, the former orientation would give higher values of hardness and Young's modulus.

Fig. 6c shows that at position #2, the modulus is ~7.5 GPa in the inner dorsal region up to a normalized distance of 0.8; the indentations are parallel to the longitudinal fibers in the inner layer. Young's modulus clearly drops in the outer layer region (5.6 GPa), because indenting on the circumferentially aligned fibers in the outer layer is perpendicular to them. This agrees well with the structural observation of the calamus. For the dorsal cortex at position #6, no outer layer is observed, and the modulus and hardness values are comparable throughout the normalized distance (detailed data in Table 1), due to solely indenting parallel to the longitudinal fibers. Fig. 6d shows that the lateral walls at position #5 show slightly smaller variation in moduli among the three indenting orientations (around 4.8 GPa, detailed values in Table 2) than the dorsal cortex. This supports the structural findings that the lateral walls are composed of crossed-fibers; thus, indenting on the three sections generates nanomechanical values that vary less than those of dorsal cortex that is dominantly composed of axial fibers. The modulus and hardness values on the dorsal and ventral regions measured here are consistent with nanoindentation reports on feather rachis [23,44], but significantly higher than those from Liu et al. [19], which may be due to indent-

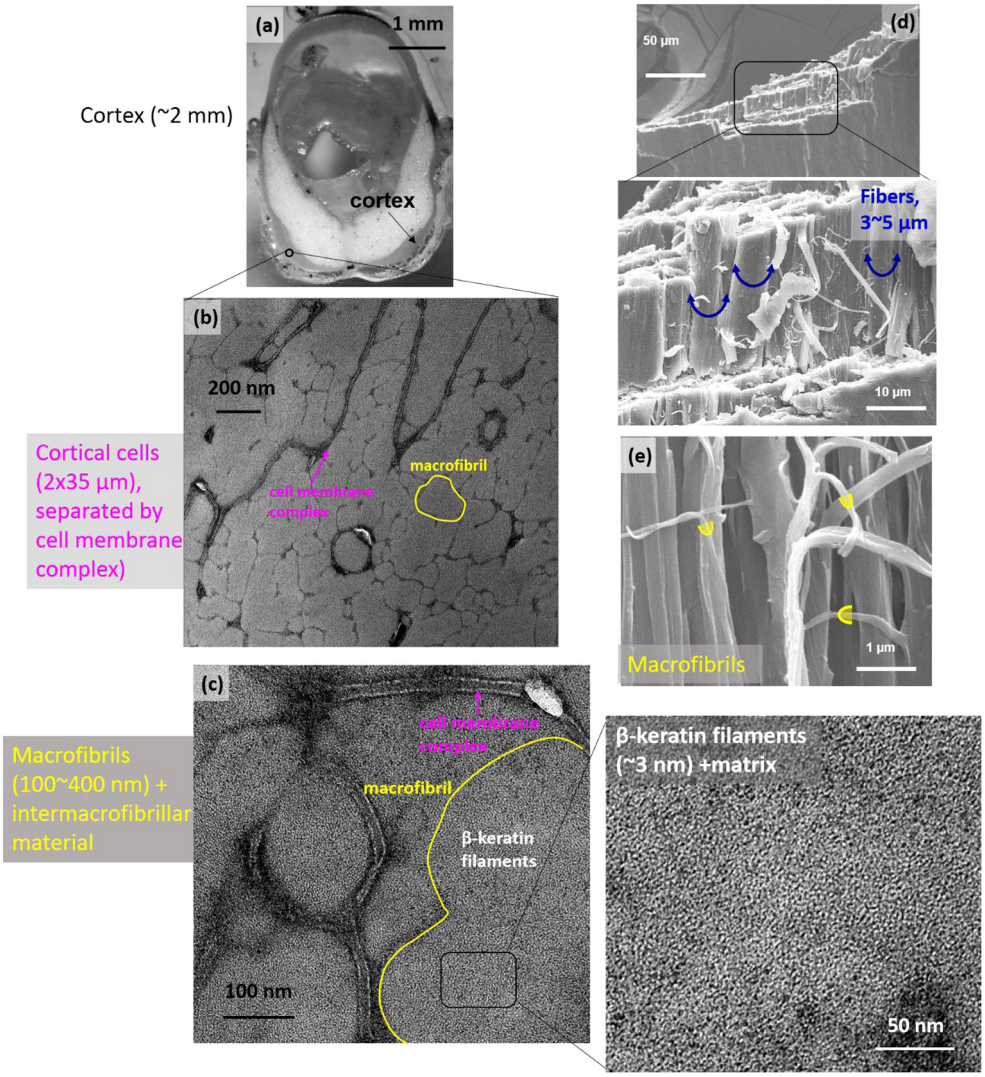


**Fig. 4.** The hierarchical fibrous structure of ventral cortex in the rachis: (a–c) transmission electron micrographs of transverse sections showing the cortex, cortical cells separated by cell membrane complex, macrofibrils outlined by intermacrofibrillar material, and β-keratin filaments embedded in matrix. Scanning electron micrographs of tensile fractured ventral strip of rachis, lateral view. (d) Axially (longitudinally) aligned bulk fibers are present, with 3–5 μm in width (blue semi-circular arrows). (e) Higher magnification image of the fibers, showing the macrofibrils (50–300 nm in diameter, yellow semi-circles), which agree with those in transmission electron micrographs. (For interpretation of the references to color in this figure legend, the reader is referred to the web version of this article.)

ing on different locations or orientations. Thus, the current nanoindentation measurements corroborate the observation of fiber orientations.

### 4.2. Tensile response

The feather cortex has anisotropic properties. Examination of the tensile response of cortex strips of dorsal, lateral, and ventral regions along the shaft length is presented in Fig. 7, and the data are summarized in Table 3. All stress-strain curves show an initial elastic region, from which the Young's modulus can be calculated, followed by a short non-linear deformation region and failure.

The dorsal cortex clearly shows increasing Young's modulus and tensile strength from the calamus to the distal shaft (37.5% and 49.5% increase, respectively), while the breaking strain does not vary much (Fig. 7a). The ventral cortex exhibits a similar trend, but not as significant. This is within expectation, since both dorsal and ventral cortex show an increasing fraction of axially aligned fibers (Section 3.2). This is consistent with reports that towards the distal shaft the volume of circumferential fibers decrease [9,10], and the Young's modulus increases [8]. However, the lateral walls show an evidently decreased Young's modulus and tensile strength (26% and 46% decrease, respectively); the breaking strain also decreases. This is due to the fact that the lateral walls change structure from circumferential fibers enclosing axial fibers at the calamus to crossed-fibers at the rachis. The fibers are not aligned with the tensile direction and therefore the strength is reduced. The lateral walls are significantly thinner than the dorsal and ventral cortex, and therefore producing more delicate specimens and larger scattering results.

In addition, at the calamus, the dorsal, ventral and lateral walls generate almost the same modulus (~3.3 GPa), strength (167.1 MPa) and breaking strain (0.12) (Fig. 7d–f), which agrees with the homogeneous two-layered fibrous structure described. At the middle shaft, the dorsal and ventral cortex are stronger and stiffer than the lateral walls since the latter are composed of crossed-fibers. The ventral cortex is slightly weaker and more compliant than the dorsal cortex, which may be due to a ventral groove being a weak point and thus prone to split before fracture. The dorsal and ventral cortex at the distal shaft show similar modulus, strength and breaking strain as a result of the constituent axial fibers, while lateral walls are much weaker and more compliant.

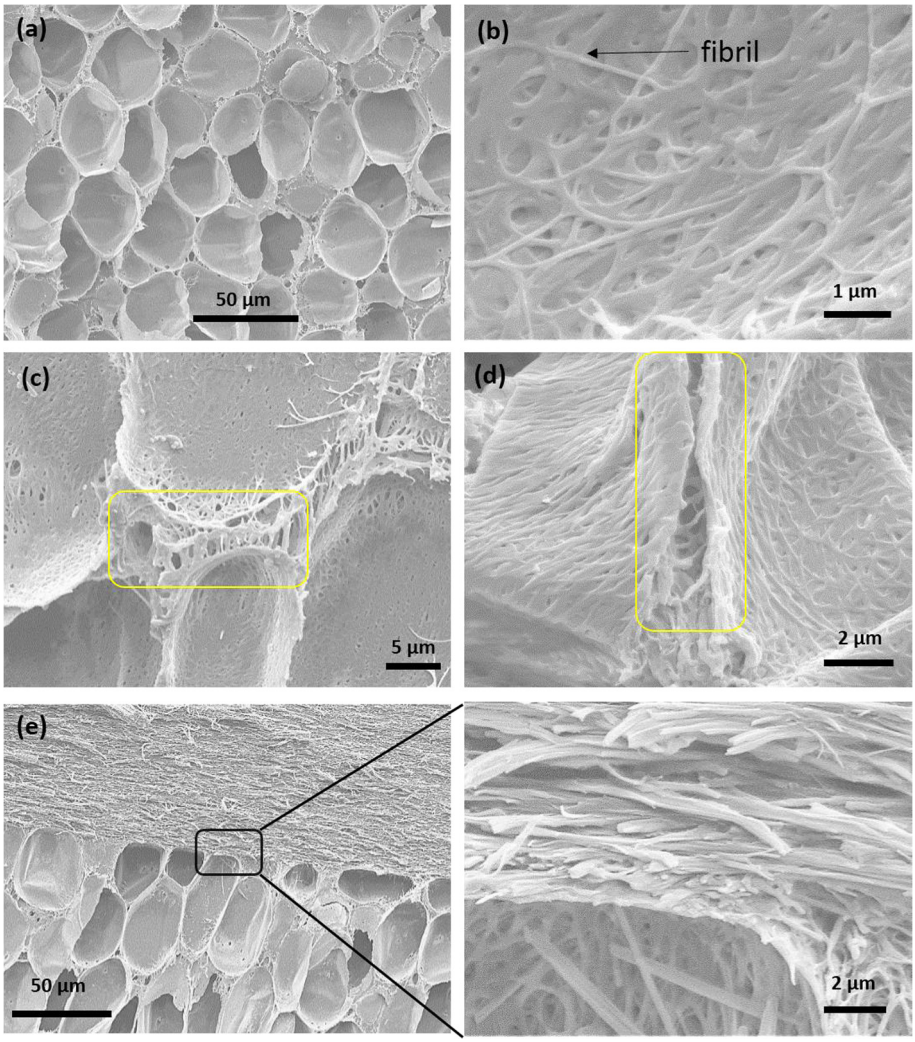


**Fig. 5.** Scanning electron micrographs of the medulla: (a) the medulla exhibits a closed-cell foam-like structure, and the cells show near round shape with about 20–30 μm in diameter; (b) higher magnification image of the cell walls reveals the fibrous and porous structure at nanoscale, arrow pointing to fibrils; (c) and (d) the fibrous struts that connect and strengthen the cell wall interfaces (yellow rectangles); (e) long-cs of distal rachis at the interface of medulla and cortex, with a higher magnification image of the area in red dotted rectangle in (e), showing that the fibrils of cell walls merge with the fibrils composing cortex. (For interpretation of the references to color in this figure legend, the reader is referred to the web version of this article.)

Being very light, the seagull feather shaft shows specific strength (density normalized) of 168 kN m/kg (using the measured density of solid keratin of 1.2 g/cm$^3$ and tensile strength of 200 MPa) that is on the same order of engineering alloys, e.g. 304 Stainless steel 65 kN m/kg, titanium alloys 100–300 kN m/kg, indicating the preeminence of being both strong and lightweight.

The deformation and fracture mechanisms also depend on the particular cortical regions and locations along the shaft length, originated from the differently aligned fibers. At the calamus, dorsal, lateral and ventral specimens all show (Fig. 8a) transverse straight fracture due to the rupture of majority axial fibers. A few splitting and axial cracks are present while circumferential fibers hold axial fibers, and there is also some delamination/peeling off of axial fibers. At the middle shaft, the dorsal and ventral regions also exhibit transverse straight fracture, whereas the lateral walls show a transverse zigzag fracture appearance (Fig. 8d). Delamination and clear axial cracks appear, but not totally detached, in the dorsal region, which is attributed to the thinner outer layer of circumferential fibers. The cracks often deflect along the cortical cell boundaries. The ventral region, composed of solely axial fibers, splits longitudinally into pieces with several fiber bundles bridging the extensive cracks. At the distal shaft, both dorsal and ventral regions show a transverse straight fracture view and a larger degree of axial splitting/cracking, with fibers peeling off or delamination. The lateral walls show a zigzagged fracture morphology, and the axial cracks are bridged and deflected due to crossed fibers (Fig. 8g).

The axial fibers rupture, creating a transverse straight fracture morphology, and tend to split axially, the degree of which depending on the existence of circumferential fibers. Axial fibers also peel off or delaminate, and sometimes show bridging effects. The circumferential fibers, present at the calamus and middle shaft, hold axial fibers together, providing good bonding, while the crossed-fibers produce a transverse zigzag fracture appearance, lead to fiber bridging, and deflect axial cracks. These differ from the flightless feather rachis where fiber rupture is the dominant failure [19].

However, it should be emphasized that in the natural environment the feathers fail mostly by flexure. This produces both compressive and tensile stresses and will be analyzed in Section 4.4.

### 4.3. Compressive behavior

#### 4.3.1. Axial compression

A quantitative analysis of the compressive behavior considering for the first time a more accurate geometry (the square cross section) and incorporating the effects of medulla is presented. Fig. 9

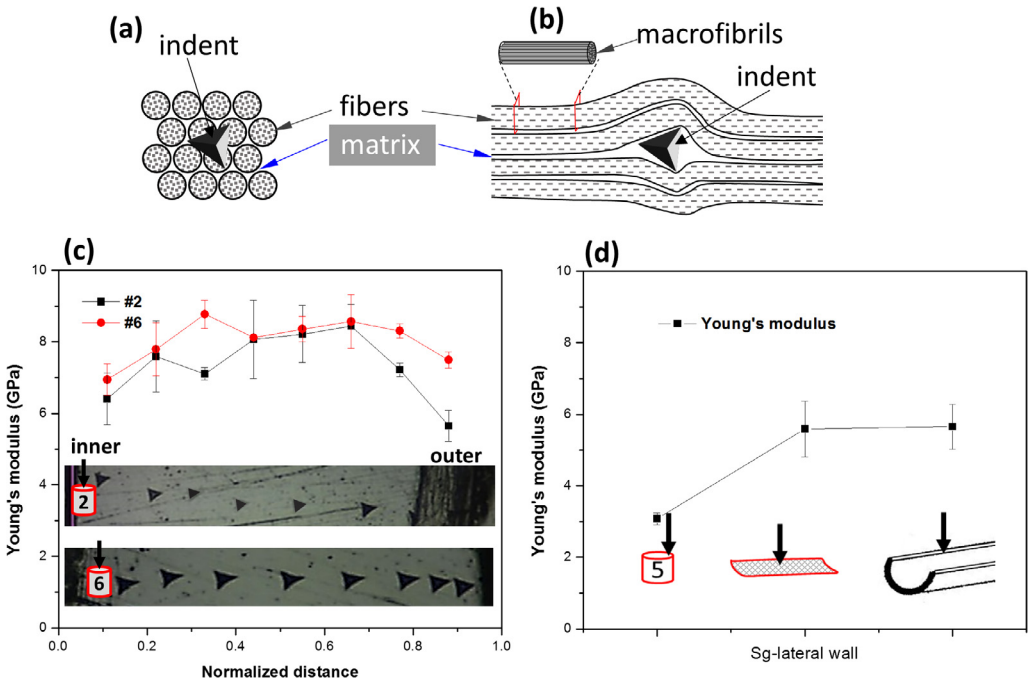


**Fig. 6.** Effect of fiber orientation on the deformation mechanisms and results. Loading (a) parallel and (b) perpendicular to the fibers (each fiber represents one fiber composed of macrofibrils). Nanoindentation on seagull feather shaft: (c) Young's moduli along the dorsal cortex thickness (normalized distance, equal to ratio of distance from inner surface to total thickness of dorsal cortex) at the calamus (position #2) and the distal shaft (position #6); (d) Young's moduli of lateral walls in different loading orientations: indenting on transverse section, on lateral wall surface, and on longitudinal section. Error bars represent standard deviations.

**Table 1**
Nanoindentation results along the dorsal cortex thickness at calamus (#2) and distal rachis (#6) of seagull feather.

| | | #2 | | 6# | |
|---|---|---|---|---|---|
| | | Hardness (GPa) | Young's modulus (GPa) | Hardness (GPa) | Young's modulus (GPa) |
| Along dorsal cortex thickness | 1st | 0.4 ± 0.1 | 6.4 ± 0.7 | 0.5 ± 0.1 | 6.94 ± 0.4 |
| | 2nd | 0.5 ± 0.02 | 7.6 ± 1.0 | 0.5 ± 0.1 | 7.79 ± 0.7 |
| | 3rd | 0.4 ± 0.02 | 7.1 ± 0.2 | 0.6 ± 0.1 | 8.77 ± 0.4 |
| | 4th | 0.5 ± 0.1 | 8.1 ± 1.1 | 0.5 ± 0.01 | 8.12 ± 0.02 |
| | 5th | 0.5 ± 0.1 | 8.2 ± 0.8 | 0.6 ± 0.1 | 8.36 ± 0.4 |
| | 6th | 0.5 ± 0.1 | 8.4 ± 0.6 | 0.6 ± 0.1 | 8.57 ± 0.7 |
| | 7th | 0.5 ± 0.1 | 7.2 ± 0.2 | 0.6 ± 0.03 | 8.31 ± 0.2 |
| | 8th | 0.4 ± 0.1 | 5.6 ± 0.4 | 0.6 ± 0.1 | 7.50 ± 0.2 |

**Table 2**
Nanoindentation results along different orientations (indenting on tran-cs, cortex surface and long-cs) at dorsal cortex and lateral wall of seagull feather.

| | | 1# dorsal cortex | | 5# lateral wall | |
|---|---|---|---|---|---|
| | | Hardness (GPa) | Young's modulus (GPa) | Hardness (GPa) | Young's modulus (GPa) |
| Along different orientations | On tran-cs | 0.5 ± 0.1 | 8.2 ± 0.6 | 0.3 ± 0.03 | 3.1 ± 0.2 |
| | On cortex surface | 0.4 ± 0.1 | 5.3 ± 0.4 | 0.4 ± 0.1 | 5.6 ± 0.8 |
| | On long-cs | 0.4 ± 0.1 | 5.2 ± 0.5 | 0.4 ± 0.1 | 5.6 ± 0.6 |

shows the axial compressive force-displacement curves of cortex, medulla and rachis (cortex enclosing medulla) and an enlarged plot for a representative medulla sample. Filling the cortex with medulla leads to significant increase in the load-bearing capacity in all specimens: forces at first peak or beginning plateau region of rachis are almost double those of cortex. In addition, cortex samples split at the ends. This axial failure advances with increasing load, and leads to a sudden decrease in load (first load drop, indicated in Fig. 9a). No sudden load drop due to splitting was observed in rachis. The medulla shows a stress-strain curve that is typical of cellular materials: a linear elastic region with ~0.02 GPa stiffness, a stress plateau correlating to the progressive compression and collapse of medullary cells, and a densification region. The maximum force is a minute fraction of that of the cortex, but the synergy is evident. The values are comparable to those of medulla reported by Liu et al. [19] and Bonser [45]. Detailed results are summarized in Table 4.

Fig. 10a–c shows the morphologies of medulla after the compressive load is removed. No significant cracks are observed, and the foam cells are clearly compressed, showing stretched morphologies perpendicular to the loading direction. The heavily bent and deformed cell edges (Fig. 10c) are not fully recovered, while the fibril bundles act as struts at cell wall interfaces and still retain good bonding. The cortex shows that axial cracking/splitting and subsequent buckling initiate from the ends, and the cracks propagate continuously (Fig. 10d). The rachis shows a strikingly different

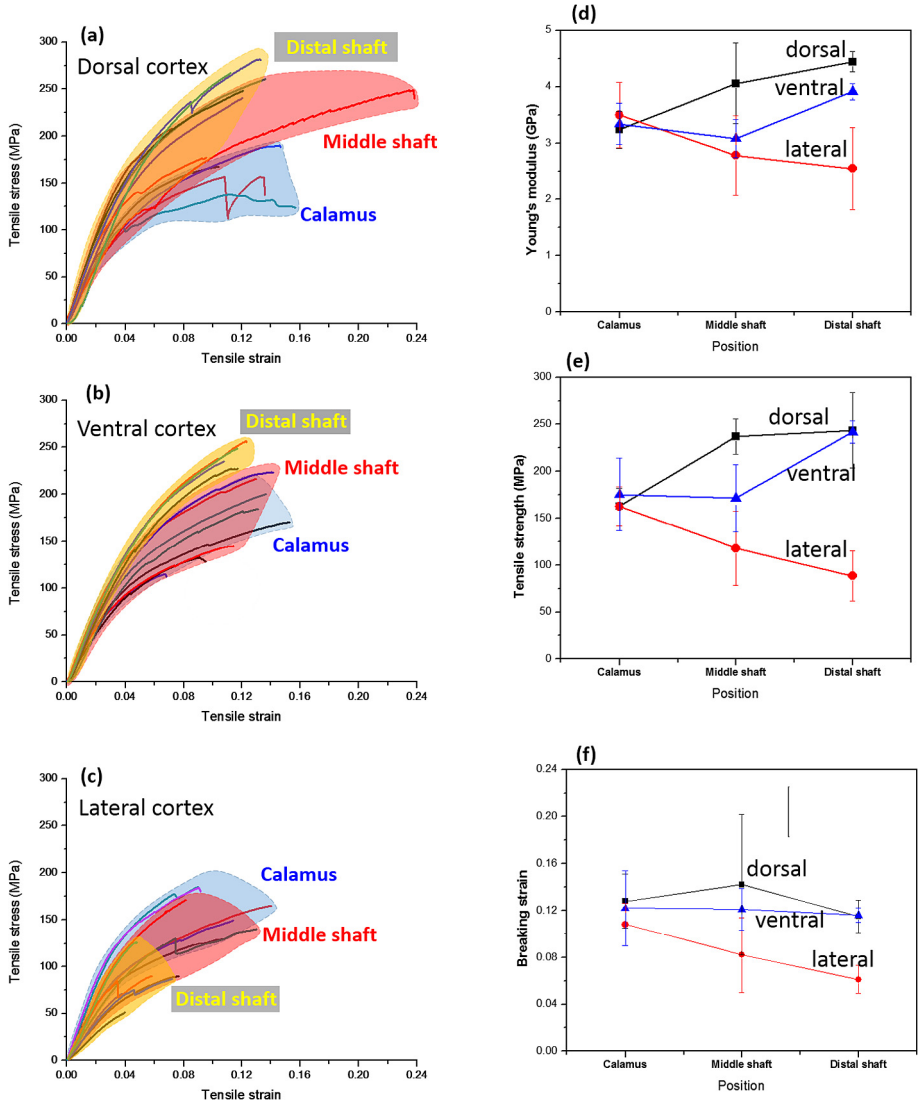


**Fig. 7.** Tensile responses of seagull cortex strips along the shaft length: stress-strain curves of (a) dorsal cortex, (b) ventral cortex, (c) lateral cortex at the calamus, middle shaft and distal shaft; variation of (d) Young's modulus, (e) tensile strength, (f) breaking strain of the dorsal, lateral and ventral cortex strips along the shaft length.

**Table 3**
Tensile results of dorsal, ventral and lateral cortex strips along the shaft length (from the calamus to the distal shaft). Errors represent standard deviations of five valid measurements.

| | | Young's modulus (GPa) | Tensile strength (MPa) | Breaking strain |
|---|---|---|---|---|
| Calamus | Dorsal | 3.2 ± 0.3 | 162.9 ± 19.1 | 0.13 ± 0.02 |
| | Ventral | 3.3 ± 0.4 | 175.3 ± 38.8 | 0.12 ± 0.03 |
| | Lateral | 3.5 ± 0.6 | 162.6 ± 21.1 | 0.11 ± 0.02 |
| Middle shaft | Dorsal | 4.1 ± 0.7 | 237.2 ± 18.7 | 0.14 ± 0.06 |
| | Ventral | 3.1 ± 0.3 | 171.3 ± 35.8 | 0.12 ± 0.02 |
| | Lateral | 2.8 ± 0.7 | 117.9 ± 39.7 | 0.08 ± 0.03 |
| Distal shaft | Dorsal | 4.4 ± 0.2 | 243.5 ± 40.2 | 0.12 ± 0.01 |
| | Ventral | 3.9 ± 0.2 | 241.9 ± 11.5 | 0.12 ± 0.01 |
| | Lateral | 2.6 ± 0.7 | 88.4 ± 26.5 | 0.06 ± 0.01 |

deformation behavior: the cortex and medulla show good bonding without obvious separation, the buckling at the end is more uniform, and there are microcracks in the wrinkled region, a toughening mechanism that absorbs energy before failure (Fig. 10e and f). In addition, the severely compressed rachis shows axial cracking/splitting, but toughening mechanisms also appear, e.g. crack deflection, ligament bridging, and fiber bridging (Fig. 10g and h). These indicate a significant increase in the buckling resistance and the toughness in the rachis due to the presence of the medulla inside the cortex.

The cortex specimens resemble a hollow square tube where each face is a rectangular plate; therefore the problem is formulated as buckling of plate elements of columns [46,47]. The buckling stress, $\sigma_{cort}$, of an axially compressed square tube is [46,47]:

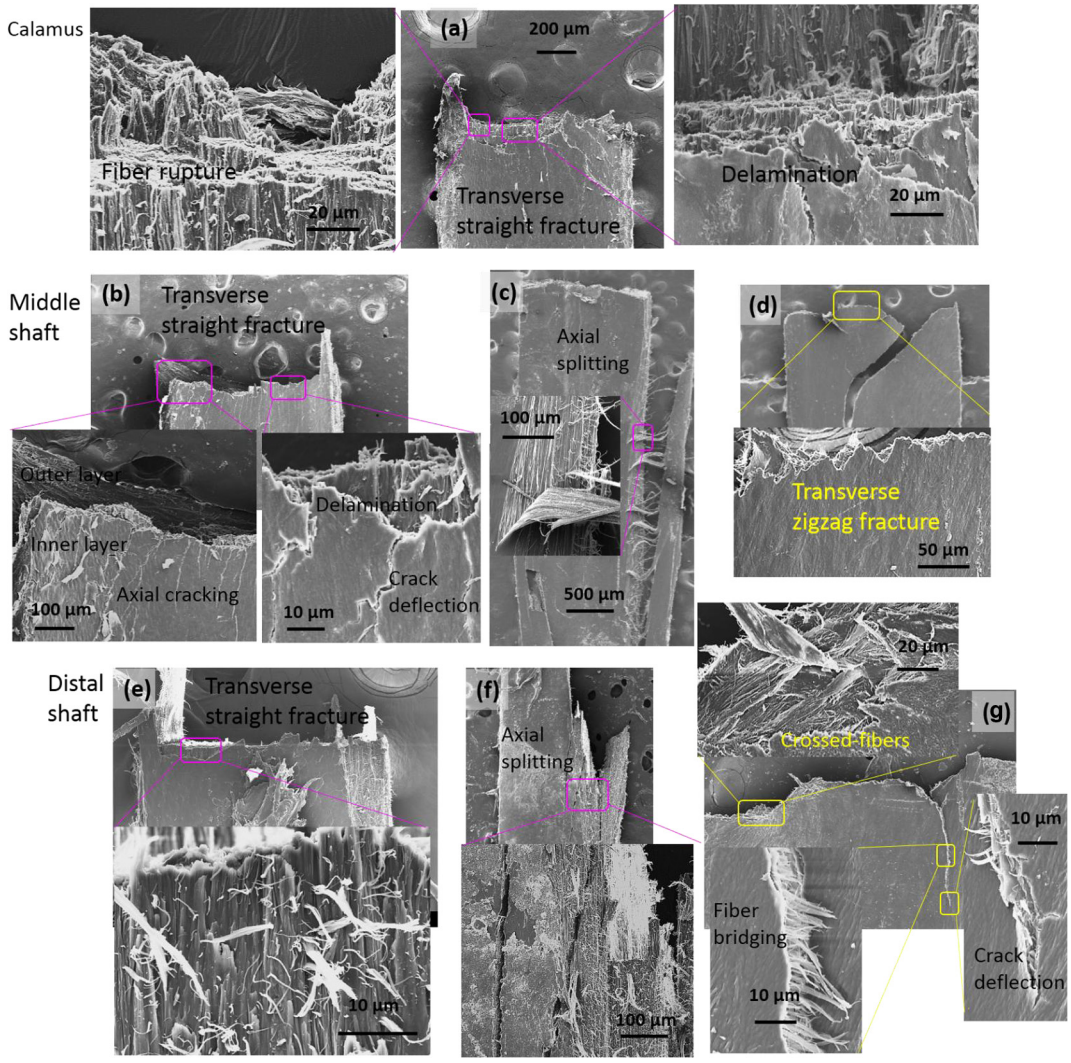


**Fig. 8.** Side views of tensile fractured cortex specimens along the shaft length: at the calamus, (a) the dorsal, lateral and ventral regions all show a transverse straight fracture due to rupture of the axial fibers, the circumferential fibers covering axial fibers, delamination and peeling off. The middle shaft (b and c) shows the same transverse straight fracture with axial cracking, crack deflection, and delamination, the ventral region (c) shows significant axial splitting, whereas (d) the lateral walls show transverse zigzag fracture due to crossed-fibers. At the distal shaft, (e and f) the dorsal and ventral regions exhibit transverse straight fracture, while (g) the lateral walls show cross fibers in layers, and clear fiber bridging and crack deflection.

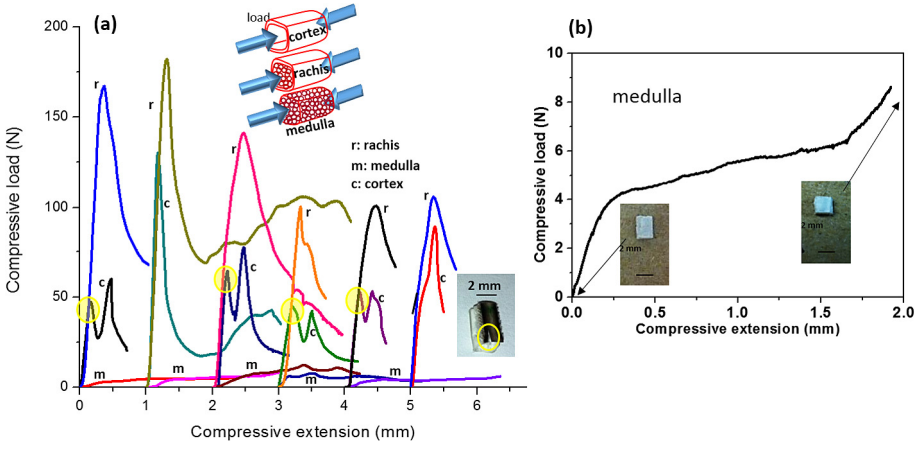


**Fig. 9.** Axial compression: (a) force-extension curves of the cortex, medulla and rachis specimens, the first load drop seen in cortex compression is due to axial splitting, indicated by yellow circles; (b) representative compressive force-extension curve of medulla. (For interpretation of the references to color in this figure legend, the reader is referred to the web version of this article.)

**Table 4**
Compressive results in axial and transverse loading orientations of cortex, medulla and rachis. Errors represent standard deviations of five valid measurements.

| | Young's modulus (MPa) | Compressive strength (MPa) | Strain at strength |
|---|---|---|---|
| Axial-cortex | 1840 ± 630 | 53.8 ± 19.9 | 0.04 ± 0.02 |
| Axial-medulla | 18 ± 12 | 1.3 ± 0.3 | 0.18 ± 0.07 |
| Axial-rachis | 452 ± 99 | 22.0 ± 4.2 | 0.07 ± 0.02 |
| Transverse-cortex | 0.9 ± 0.5 | 0.1 ± 0.04 | 0.15 ± 0.05 |
| Transverse-medulla | 3.6 ± 0.9 | 0.7 ± 0.2 | 0.26 ± 0.06 |
| Transverse-rachis | 19.9 ± 6.8 | 1.3 ± 0.4 | 0.09 ± 0.04 |

$$\sigma_{cort} = \frac{\pi^2 E}{3(1-\nu^2)}\frac{t^2}{a^2} \quad (1)$$

where $E$, $a$, $t$ and $\nu$ are the elastic modulus, side width of the square tube, tube thickness, and Poisson's ratio. Substituting in the corresponding values, 4 GPa, 2.17 mm, 0.142 mm and 0.3 from ax-cortex-no. 3 specimen, we obtain a buckling stress of 61.7 MPa, which is in strong agreement with the experimental result of this specimen, 58.1 MPa; in contrast, the only reported compressive strength of feather cortex based on a cylinder is 136.5 MPa versus an experimental value of 92.4 MPa [19]. For a thin-walled hollow circular tube, the axial buckling strength is $\sigma^{cir} = \frac{E}{\sqrt{3(1-\nu^2)}}\frac{t}{r}$, where $r$ is the radius of the tube [15]. To compare with that of empty square tube, we assume the same cross sectional area, which gives $4a = 2\pi r$. Then a circular tube locally buckles in axial compression at a stress of about $0.6E(t/r)$ while a square tube buckles at $3.6E(t/a)^2$ ($\nu = 0.3$ for both cases, $t/a \ll 1$). Therefore, the circular tube has a higher buckling stress than the square one.

The cellular medulla has a closed-cell foam structure, with fibrous and porous cell walls. The relative Young's modulus (modulus of medulla over that of solid) is obtained from Gibson and Ashby's equation [38]:

$$\frac{E_m}{E_s} = \varphi^2\left(\frac{\rho_m}{\rho_s}\right)^2 + (1-\varphi)\frac{\rho_m}{\rho_s} + \frac{P_0(1-2\nu_m)}{E_s\left(\frac{\rho_s-\rho_m}{\rho_s}\right)} \quad (2)$$

where $E_m$ and $E_s$ are the Young's moduli of medulla and the solid cortex ($m$ and $s$ denote medulla and solid). ρ is the density, $\varphi$ the volume fraction of solid contained in the medullary cell edges, and $\nu$ the Poisson's ratio (0.33). $P_0$ is the gas pressure which is expected to be atmospheric pressure (~0.1 MPa), and this third term can be neglected since the pressure effect of foam induced from compression is negligible. Calculating the relative density [38] by comparing the shape of cells from SEM images of medulla, one obtains $\frac{\rho_m}{\rho_s} = 0.11$. $E_s$ is 4 GPa from tensile tests on rachis cortex, $\varphi$ is calculated by using the tetrakaidecahedra cells, being 0.703 [38]. Substituting these values, the estimated $\frac{E_m}{E_s}$ is 0.0386. Taking compressive moduli from compression tests of cortex and medulla, the ratio of modulus of medulla over that of cortex is 0.010

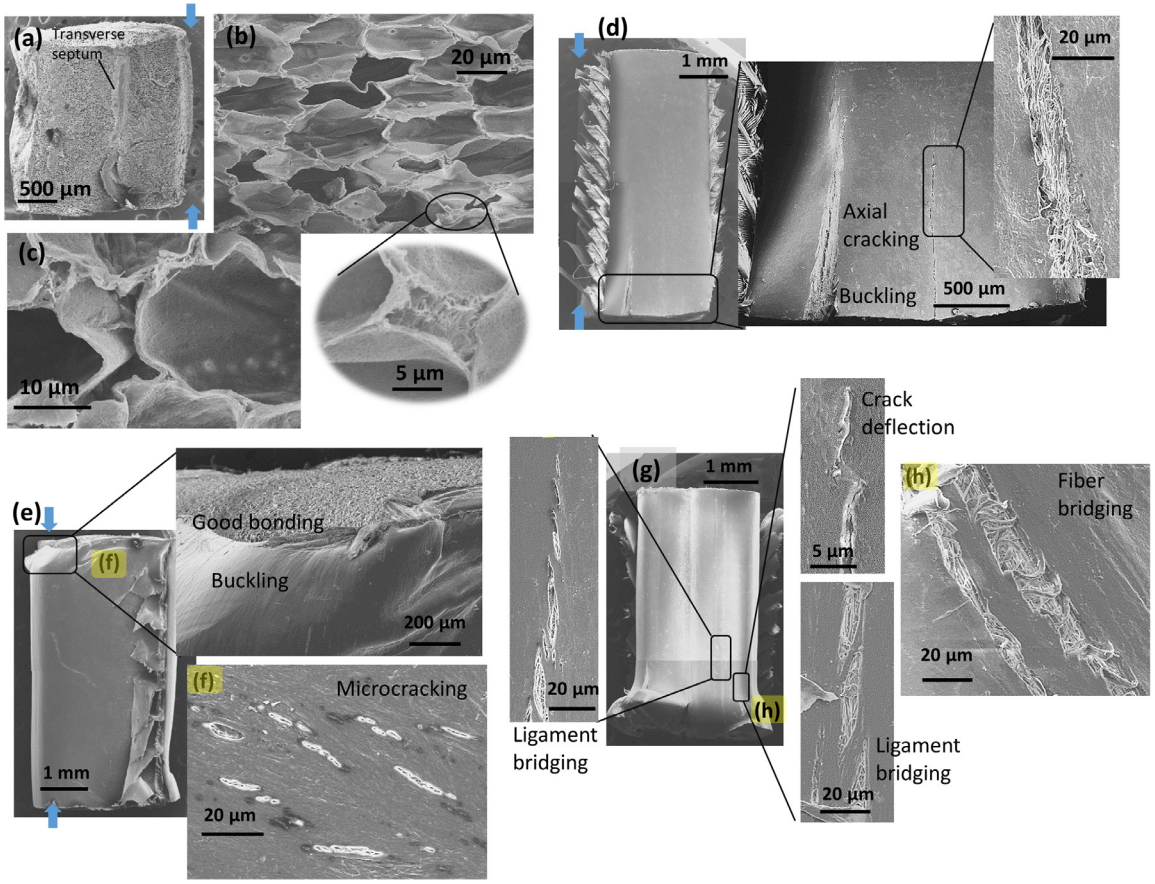


**Fig. 10.** Scanning electron micrographs of specimens after compressive force removed: (a) medulla sample (blue arrows indicate loading direction), (b) medullary cells showing deformed shape along horizontal direction, while the fibril bundles at the cell interface remain connected; (c) higher magnification image of the deformed cell edges. (d) Cortex specimen showing axial cracking and buckling. (e and f) Compressed rachis specimen showing uniform buckling at the end and microcracking in the wrinkled region. (g and h) Severely compressed rachis specimen with axial splitting, and toughening mechanisms. (For interpretation of the references to color in this figure legend, the reader is referred to the web version of this article.)

(0.018 GPa/1.84 GPa, from compressive measurements). It is possible that damage to the medulla was introduced during specimen preparation. In addition, the cell walls are fibrous and porous, which should be weaker than the solid cell walls assumed in the equation. The relative modulus of seagull father rachis is larger than that of peacock's tail feather (0.00458) [19], but comparable to that of porcupine quills [48]. The seagull feather medulla shows cell faces that have a thickness comparable to cell edges, and has fibrous struts at most cell interfaces (Fig. 5c and d). These features stiffen the medulla to resist loading and deformation, thus generating a higher value of relative modulus.

The rachis, considered as a square tube filled with a foam core under compressive loading, can be modeled as rectangular plates supported by an elastic foundation and subjected to in-plane axial compression [49,50]; this is shown in Fig. 11 with parameters. Including effects of the foundation into the buckling of the plate and assuming a sinusoidal function for the deflection, the in-plane compressive force $N_x$ is given as [50]:

$$N_x = D\left(\frac{\pi}{a}\right)^2\left[\left(\frac{ma}{l}\right)^2 + 2 + \left(\frac{l}{ma}\right)^2\left\{1 + \frac{k}{D}\left(\frac{a}{\pi}\right)^4\right\}\right] \quad (3)$$

where $a$ and $l$ are the side width and length of the square tube, $D = \frac{Et^3}{12(1-\nu^2)}$, $k$, and $m$ are the flexural rigidity of plate, stiffness of foundation $k = \frac{2E_m}{a}$, and the number of half sine waves along the plate.

For a given square tube, the buckling force occurs at $\frac{\partial N_x}{\partial m} = 0$ with a certain integer value of $m = m^* = \frac{l}{a}\left\{1 + \frac{k}{D}\left(\frac{a}{\pi}\right)^4\right\}^{\frac{1}{4}}$. Substituting this into Eq. (3) we obtain the buckling load:

$$N_x = 2D\left(\frac{\pi}{a}\right)^2\left[\sqrt{1 + \frac{k}{D}\left(\frac{a}{\pi}\right)^4} + 1\right] \quad (4)$$

This expression is in agreement with the equation presented by Moradi and Arwade [51] derived from Seide [52]. Therefore, the buckling stress for a square tube with a foam core is:

$$\sigma_{cr}^{comp} = \frac{N_x}{a/2} = 4D\frac{\pi^2}{a^3}\left[\sqrt{1 + \frac{k}{D}\left(\frac{a}{\pi}\right)^4} + 1\right] \quad (5)$$

Substituting in E = 4 GPa, $\nu$ = 0.3, t = 0.142 mm, a = 2.17 mm, $E_m$ = 0.018 GPa of ax-rachis-no. 3, one can calculate the buckling stress to be 12.71 MPa. Comparing with the experimental value of this specimen, 27.3 MPa, the rachis shows significantly higher compressive buckling stress than that predicted from Eq. (5) (115% increase), indicating a synergistic effect in strengthening between the medulla and cortex. Firstly, Eqs. (3)–(5) are based on the Winkler foundation [53], which is composed of a series of isolated elastic springs without interactions between them (Fig. 10c). In the rachis, the medullary cells (the foundation) are closely connected by cell edges and faces and strengthened by fibrous struts at cell interfaces. This creates an intrinsically strengthened foundation and thus an enhanced bracing of the medulla to the cortex, therefore increasing the buckling resistance of the rachis. In addition, the plate on elastic foundation model (Fig. 10c) assumes a rigid attachment, which may detach upon loading. In the rachis, the interface of cortex and medulla shows fibrils well merged into each other (Fig. 5f), which leads to good bonding at the interface even after buckling deformation. Also, the foamy medulla not only alleviates axial splitting but also introduces several crack-shielding mechanisms, including microcracking, crack deflection, ligament and fiber bridging. And the lateral walls in the rachis help constrain the buckling of the top plate. All of these contribute to the enhanced strength and stiffness of the composite rachis.

Furthermore, the foam-filled rachis can be analyzed through the classic sandwich panel theory; the buckling failure is 'wrinkling', and the compress stress in the cortical shell at which wrinkling occurs is $\sigma_s = 0.57E_s^{\frac{1}{3}}E_m^{\frac{2}{3}}$ (Poisson's ratio of 1/3 for medulla) [54]. Substituting $E_s$ = 4 GPa, and $E_m$ = 0.0386Es, $\sigma_s$ = 260.4 MPa. Considering the same rachis specimen (ax-rachis-no. 3), the measured cortical area is 1.1 mm$^2$ and the force at buckling is 141.2 N; the stress in the solid shell, estimated by dividing the buckling force by cortical area, is 128 MPa, which is much lower than the estimated value. The elastic modulus of cortex in axial compression is lower than that in tensile; the fiber orientations and experimental damage introduced during specimen preparation may account for the difference.

It is helpful to compare the analysis with that of a circular foam-filled tube. The axial buckling stress of a circular tube filled with an elastic core is given as: $\sigma_{cr} = \frac{Et}{r}f_1$ [17,55], where $f_1$ is a function of $r/t$, $E_m/E_s$, and $\lambda_{cr}/t$, and $\lambda_{cr}$ is the half buckled wavelength divided by $\pi$. Considering a same cross sectional area in the solid for this circular tube ($4a = 2\pi r$) and substituting in relevant values, $f_1$ = 0.92, and $\sigma_{cr}$ is 375 MPa, which significantly overestimated the buckling stress of the square-shaped rachis in axial compression.

#### 4.3.2. Transverse compression

Fig. 12a shows the transverse compressive stress-strain curves of cortex, medulla and rachis; values are in Table 4. All exhibit much lower modulus and strength than those loaded axially, the Young's moduli of cortex, medulla and rachis being 0.91, 3.56 and 19.91 MPa, respectively. This is understandable, since in the

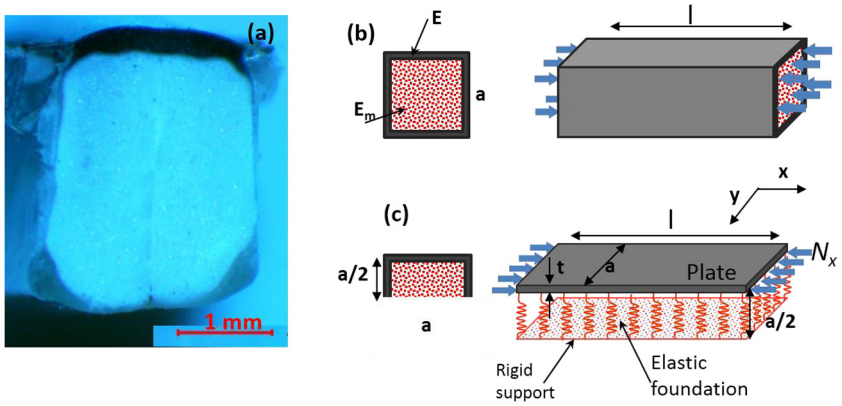


**Fig. 11.** Axial compression model: (a) image of transverse section of one specimen; (b) schematics of the square tube with a foamy core under axial loading; (c) schematics of the plate supported by an elastic foundation under in-plane compressive loading.

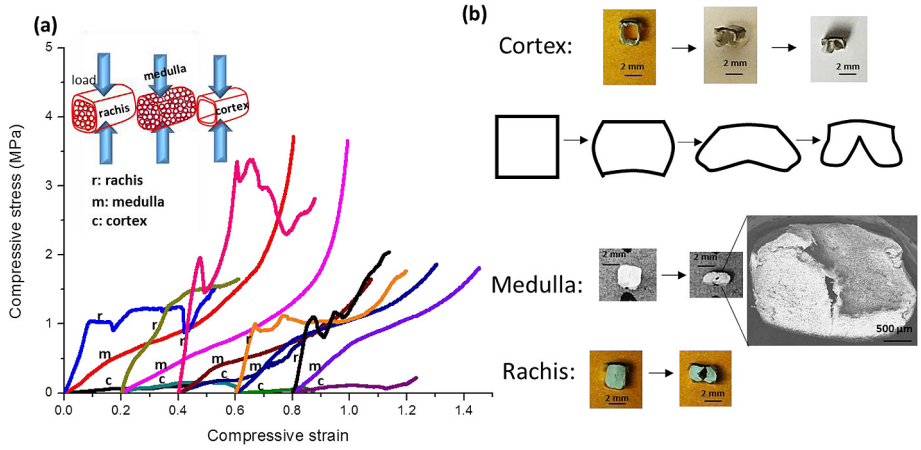


**Fig. 12.** Transverse compression: (a) stress-strain curves of rachis, medulla and cortex specimens; (b) deformation mechanisms of cortex, medulla and rachis.

real natural system, the feather rachis bends and undergoes primarily maximum axial compression on either the dorsal or ventral side, whereas purely transverse compression is not that common. One salient feature is that the foamy medulla substantially increases the load-bearing capacity of the cortex; the Young's modulus and strength increase by factors of 20 and 13, respectively, from cortex to rachis, indicating the significant strengthening effect of medulla transversely. It is also reported for the peacock tail feather rachis, the foamy medulla takes up to 96% of the total force, leaving 4% to the cortex [13].

The cortex, under transverse compression, is mainly supported by thin lateral walls composed of crossed fibers that are less stiff, and thus easily deform and buckle, as seen in Fig. 12b. The buckling load can be calculated considering the compatibility of vertical and horizontal walls (Supplementary Material II). In axial compression, the load is supported by axial fibers in the thick dorsal and ventral cortex plus crossed-fibers in lateral walls, thereby having much higher stiffness and strength. Nevertheless, no obvious cracking or breaking is observed; the lateral walls deform substantially and roll into the hollow core, a different mode from the buckling and collapse of hollow square aluminum tubes [56].

The medulla shows similar stress-strain behavior in transverse and axial compression, but exhibits significantly lower modulus (3.56 MPa) and strength (0.70 MPa). The medullary cells are near circular with similar dimensions in both transverse and longitudinal sections. Splitting in the medulla along transverse septum dorsal-ventrally occurs for most specimens (4/5), Fig. 12b; this accounts for the lower stiffness. The transverse septum (Fig. 2a) starts from ventral cortex towards, not reaching the dorsal cortex. In axial compression, however, no splitting along transverse septum was observed; the septum, present throughout the height of axially compressed specimens, buckles but does not split (Fig. 10a). Therefore, the transverse septum exhibits a stiffening and strengthening function axially, leading to stiffer and higher strength in axial compression. The composite rachis specimens, with much improved stiffness and strength, exhibit splitting along transverse septum (Fig. 12b), but remain connected at the dorsal and ventral cortex.

### 4.4. Four-point flexure

#### 4.4.1. Flexural behavior of the shaft as a composite beam

The feather shaft is a quintessential complex composite beam: a hollow cylinder at the calamus and a square shell-over-foam at the rachis. The flexural stiffness of a specimen with constant cross section is:

$$S = F/\delta \tag{6}$$

within initial linear region, where $F$ is the measured force and $\delta$ the deflection. The flexural rigidity in four-point bending is [57]:

$$K = (EI)_{comp} = \frac{dF}{d\delta}\frac{a}{48}(3L^2 - 4a^2) \tag{7}$$

where $L$ is the support span, and $a$ the distance between one loading point and its nearest support point ($a = L/4$), with the subscript *comp* representing composite. The calamus resembles a hollow cylinder and the middle and distal shaft can be considered as sandwich beams; therefore, the maximum normal flexural stress in the cortex is [38,54]:

$$\sigma_s = \frac{McE_s}{(EI)_{comp}} = \frac{FacE_s}{2(EI)_{comp}} \tag{8}$$

where $M$ is the bending moment, $E_s$ is the tensile elastic modulus of ventral cortex along the shaft length, and $c$ is half of the specimen depth. The flexural strain can be calculated from measured deflection, according to the ASTM D6272, by:

$$\epsilon = 4.36\frac{2c\delta}{L^2} \tag{9}$$

The flexural stiffness and flexural rigidity of specimens along the shaft length, calculated from experimental measurements using Eqs. (6) and (7), are shown in Fig. 13a. From the calamus to the distal shaft, both the flexural stiffness and flexural rigidity decrease, especially the latter decreases by 88%. Towards the distal shaft, the cortex size decreases significantly; this leads to significant reduce in the area moment of inertia of the composite, although foamy medulla fills the inside cortex, which overrules the increase in Young's modulus of cortex (from tensile tests) and results in decreased flexural rigidity. Fig. 13b–d shows flexural stress-strain curves of the cortices in calamus, middle and distal shaft. Towards the distal end, both the slope and the flexural strength of cortex increase; the failure stress increases from 69.1 to 113.4 MPa (Table 5). This can be understood from the fibrous structural change in cortex (volume fraction of axially aligned fibers increase in the dorsal and ventral cortex towards the distal end) and the mechanical support from the medulla to the cortex. These are the first reported flexural properties incorporating medulla and the failure stress of cortex along the feather shaft length.

From the perspective of materials design and analysis, the composite beam (solid shell over porous core) can be considered as "one material" with its own set of properties, thus allowing comparison along the shaft length and with engineering materials

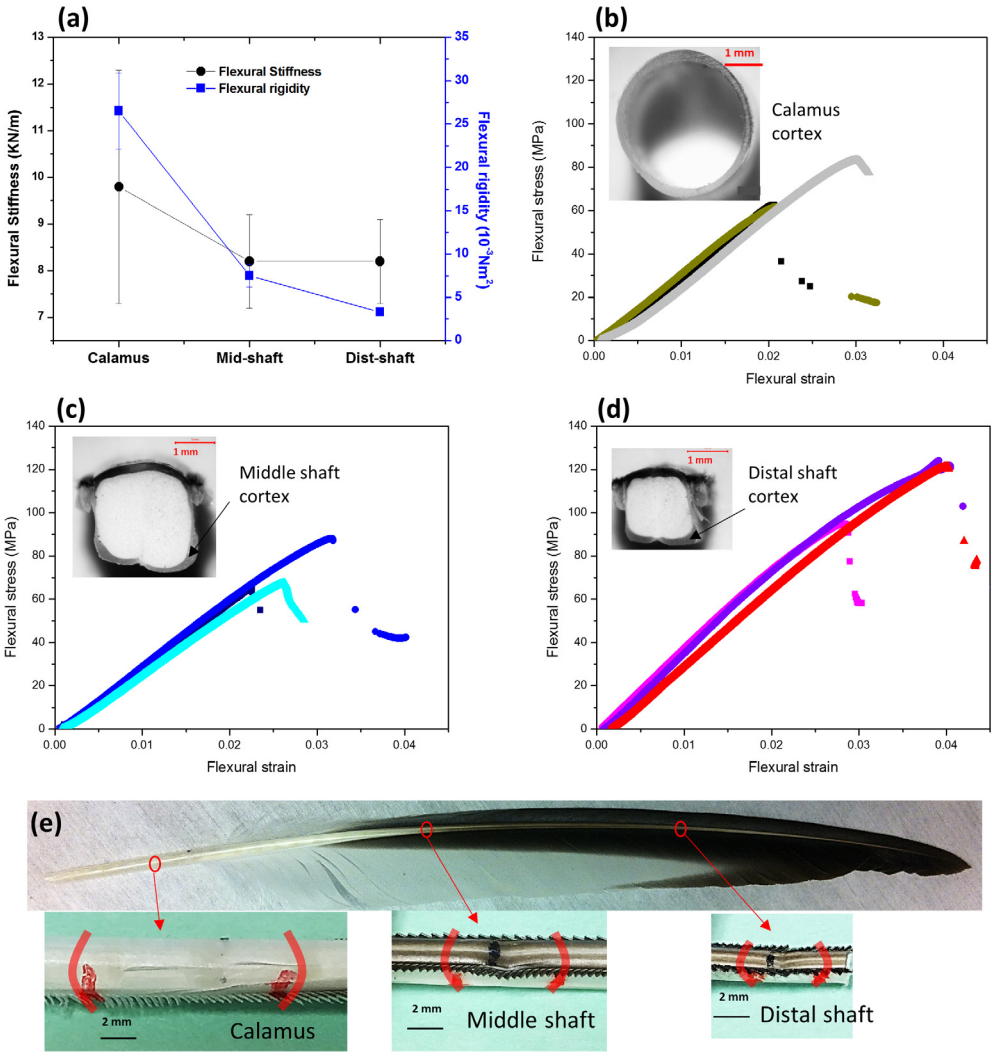


**Fig. 13.** Four point bending results: (a) flexural stiffness and flexural rigidity along the shaft length; flexural stress-strain curves of the (b) calamus cortex, (c) middle shaft cortex and (d) distal shaft cortex, with corresponding sectional views; (e) local buckling failure during flexure at the calamus, middle shaft and distal shaft.

[58]. We define an equivalent homogeneous material for each specimen that has an equivalent density (total mass divided by total volume, $\tilde{\rho}$), an equivalent flexural modulus [58]:

$$\tilde{E} = \widetilde{EI}/\tilde{I} \tag{10}$$

where $\widetilde{EI} = (EI)_{comp}$, same as that obtained from Eq. (7), and $\tilde{I}$ is obtained using SolidWorks by tracing the profiles of the entire section at the middle of each specimen, and an equivalent flexural strength:

$$\tilde{\sigma}_{flex} = M_f c/\tilde{I} \tag{11}$$

where $M_f$ is calculated from measured force at failure, $M_f = \frac{F_f a}{2}$.

The equivalent density can be calculated through:

$$\tilde{\rho} = \rho_s f_s + \rho_m f_m \tag{12}$$

**Table 5**
Four point bending results of the feather shaft (errors represent standard deviations).

| | Flexural stiffness (kN/m) | Flexural rigidity ($10^{-3}$ N m$^2$) | Flexural strength in cortex (MPa) |
|---|---|---|---|
| Calamus | 9.8 ± 2.5 | 26.5 ± 4.4 | 69.1 ± 10.0 |
| Mid-shaft | 8.2 ± 1.0 | 7.5 ± 1.3 | 73.5 ± 10.3 |
| Dis-shaft | 8.2 ± 0.9 | 3.3 ± 0.3 | 113.4 ± 13.2 |

where $f_s$, $f_m$ are averaged area fractions of the solid cortex and medulla of cross sections of the shaft. At the calamus, the density equals that of the solid cortex ($\rho_s$); for the rachis region, $\frac{\rho_m}{\rho_s} = 0.11$ from Section 4.3. Since $f_m = 1 - f_s$, $\tilde{\rho} = 0.89\rho_s f_s + 0.11\rho_s$. The area fractions of cortex along the shaft length, $f_s$, calculated by obtaining areas of cortex and medulla at each position using Solidworks via tracing profiles, are 1.0, 0.236, 0.260. Using them, the densities at the middle and distal shaft are $0.32\rho_s$ and $0.34\rho_s$, respectively. By establishing the geometry of the calamus via micrographs and measuring the weight, one obtains $\rho_s = 1200$ kg/m$^3$; therefore, the equivalent densities at middle and distal shaft are 384 and 408 kg/m$^3$ (Table 6) for the seagull feathers studied here. From the calamus to the distal shaft, as shown in Table 6, the equivalent flexural modulus and the equivalent flexural strength decrease at the middle shaft, and then increase at the distal shaft. This is due to mainly the large area occupied by the medulla, which has low modulus and does not contribute significantly to the bending stiffness.

It seems that the flexural properties decrease, or do not increase much, from the calamus to the distal shaft. However, taking into consideration equivalent density, the flexural efficiency, the specific equivalent flexural modulus and strength (equivalent flexural modulus and strength divided by corresponding equivalent density), increases remarkably towards the distal shaft (by factors of

**Table 6**
Equivalent flexural properties (considering each specimen as a homogeneous material) along the feather shaft (errors represent standard deviations).

| | Equivalent density ($kg/m^3$) | Equivalent flexural modulus (GPa) | Equivalent flexural strength (MPa) | Specific equivalent flexural modulus (MN m/kg) | Specific equivalent flexural strength (kN m/kg) |
|---|---|---|---|---|---|
| Calamus | $\rho_s = 1.2 \times 10^3$ | 5.8 ± 1.5 | 120.6 ± 13.6 | 4.8 ± 1.3 | 100.5 ± 11.4 |
| Mid-shaft | $0.32\rho_s = 384$ | 2.8 ± 0.3 | 66.6 ± 9.4 | 7.4 ± 0.8 | 175.3 ± 24.9 |
| Dis-shaft | $0.34\rho_s = 408$ | 4.4 ± 0.3 | 127.4 ± 22.4 | 10.6 ± 0.8 | 310.8 ± 54.7 |

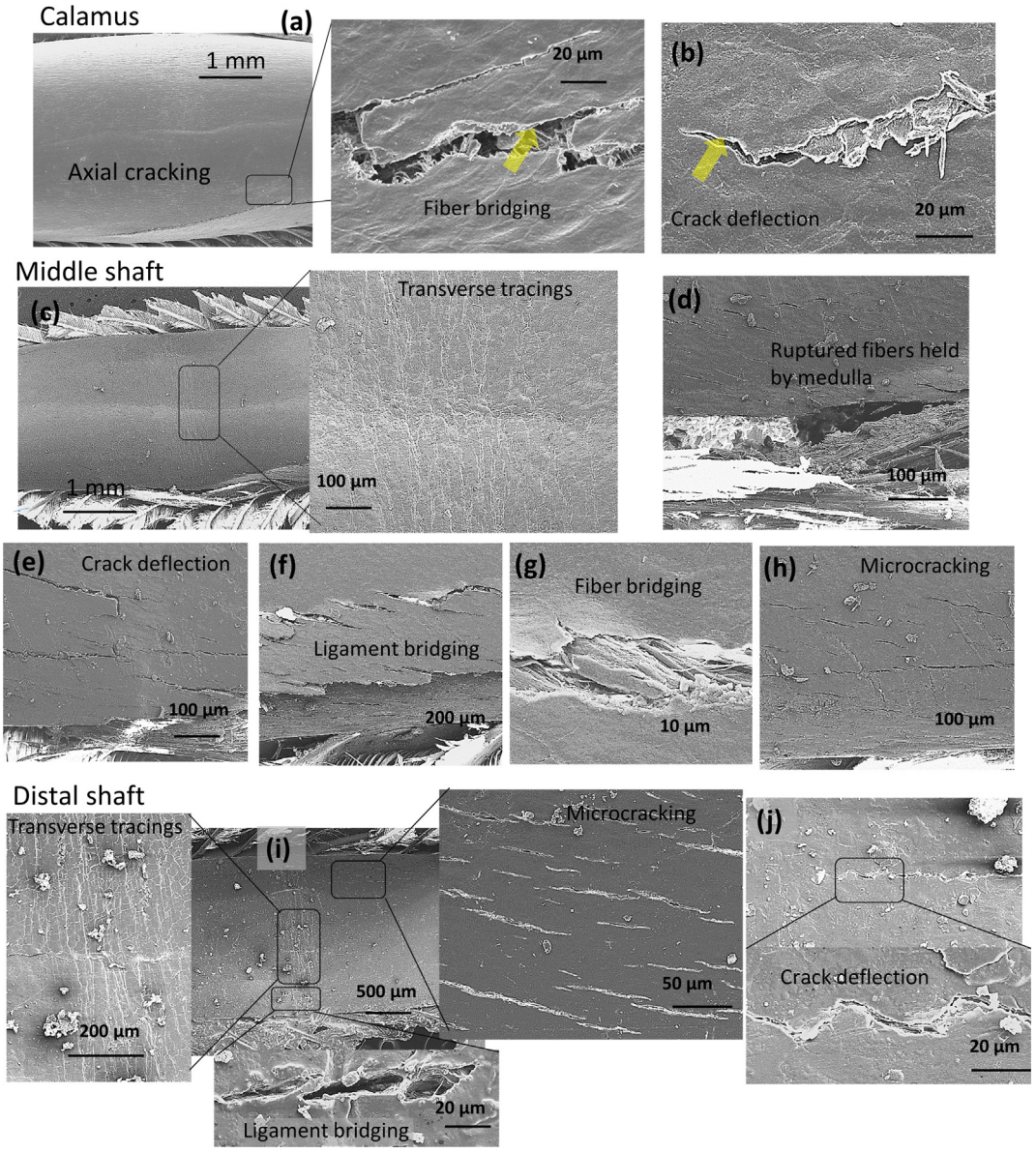


**Fig. 14.** The dorsal views of the buckled feather shaft along the shaft length: (a and b) the calamus, showing significant axial cracking and minor crack deflection and fiber bridging (indicated by arrows); (c–h) the middle shaft, showing transverse tracings at the buckled region, and ruptured fibers held by the medulla, crack deflection, ligament and fiber bridging, and microcracking; (i and j) the distal shaft with similar features as those in the middle shaft.

2 and 3, respectively), shown in Table 6. This indicates a distinguishing feature that symbolizes the design nature of feather shaft: the substantial attenuation of shaft to reduce profile drag is subtly compensated through mechanical efficiency, e.g. the shape factor changing from circular to square, the increasing volume fraction of axially aligned cortical fibers, and the presence of the medulla that increases the buckling resistance of the cortex and meanwhile lightens the shaft. Besides, the distal shaft in current study shows specific equivalent flexural strength of 310.8 kN m/kg, which is even higher than that of stainless steel (71% Fe, 18% Cr, 8% Ni, <0.2% C) in bending, 247 kN m/kg (yield strength in bending of 1.98 GPa with a density of 8.0 × 103 kg/m [59,60]).

Additionally, the feather rachis employs structural features that allow reasonable twisting when encountered large forces. The hollow square shape, providing lower torsional resistance than that of a circular one (same cross sectional area), shows a slightly

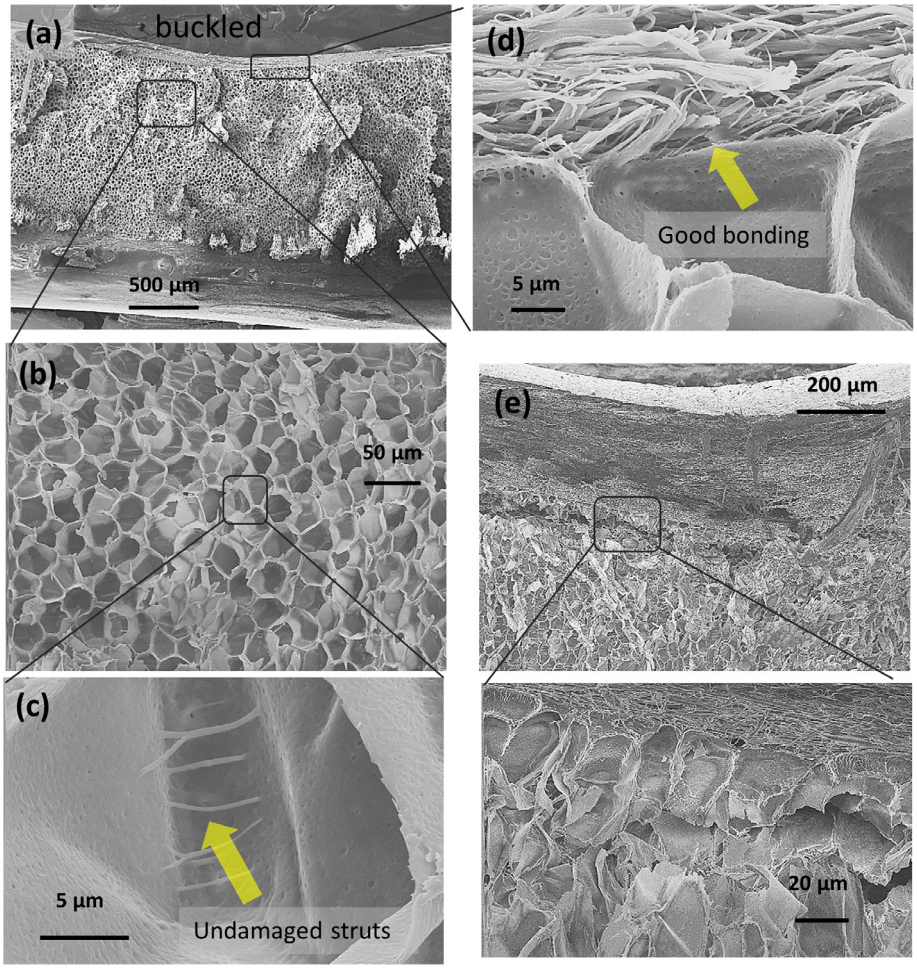


**Fig. 15.** Sectional views of the buckled feather rachis: (a–c) the medullary cells retain mostly original shape and show undamaged fibrous struts at inter-cell walls. (d) The bonding between medulla and cortex remains integrate. (e) The apparent separation within foamy medulla (below the cortex) is indeed very shallow, and the cells remain connected.

shorter height on one lateral wall and has dominant constituent axial fibers in dorsal and ventral cortex, which permit torsional deformation. This is balanced by the crossed fibers in the lateral walls that increases torsional rigidity by aligning along the direction (±45° to the shaft axis) where a twisted shaft would fail.

*4.4.2. Flexural failure mode*

The feather shaft specimens fail in four-point bending by local buckling on the compressive side (dorsal cortex) at the load drops on the flexural stress-strain curves (Fig. 13b–e). The calamus specimens collapse suddenly with significant axial cracking (Fig. 13d), exhibiting ~35% load drop. The middle and distal shaft show a reduced load drop (16–19%) and indents on the dorsal surface. Therefore, filling the core of cortex with medulla could reduce the risk of sudden failure, and thus prevents the catastrophic collapse of the structure, which is more likely to be experienced by the distal shaft which does not have a supporting skin.

The feather shaft show different mechanisms accompanying flexural failure along the shaft length. The calamus exhibits several extensive axial cracks with slight fiber bridging and crack deflection (Fig. 14a and b). The middle shaft shows numerous transverse tracings on the dorsal buckled region caused by the compressive stresses experienced locally during flexure (Fig. 14c), typifying local buckling; a small amount of fibers at the edge rupture, but are still held by the internal foamy medulla (Fig. 14d). In addition, the middle shaft, supported by the inner medulla, shows evidence of crack deflection (Fig. 14e), uncracked ligament bridging and fiber bridging (Fig. 14f and g), and abundant microcracking (Fig. 14h) near the buckled region. The distal shaft shows similar deformation features near the buckled region, e.g. transverse tracings, microcracking, crack deflection, and uncracked ligament bridging (Fig. 14i and j). These notable toughening mechanisms contribute to the load bearing capacity of the shaft and enhance the energy absorbance by allowing a considerable amount of deformation before failure; they originate from the inner foamy medulla which shares the forces and holds the fibers composing the solid cortex together, analogous to the toughening mechanisms observed in axial compression, thus preventing extensive axial cracking and splitting of the cortex in the calamus.

Another remarkable feature is the outstanding shape recovery of medulla even after the shaft fails/buckles. Fig. 15 shows the sectional views of buckled rachis. Under the buckled dorsal cortex region (the indent on the dorsal surface, Fig. 15a), the medullary cells throughout the inside space show the original normal shape and the intact strengthening fibrous struts between cell walls (Fig. 15c). For a severely buckled rachis specimen which involves a small amount of ruptured fibers held by medullary cells, observation at higher magnification reveals that the seemingly separation of medulla along cortex is rather shallow (less than one cell diameter) and the medullary cells remain connected inside (Fig. 15e). This is mainly due to the nature of sandwich structure: the stresses developed in the cellular core decay with increasing depth into the

foundation [54]. For a buckled strip supported by an elastic foundation, the stresses in the core decrease to ~5% of the maximum value at a depth of 1.6 half wavelengths [17]. Also, the hierarchical fibrous and porous structure being exceptionally deformable and lightweight contribute to this property. Other biological cellular structures with solid cell walls, e.g. porcupine quills [17], are similar to the father shaft. In addition, along the interface the cellular medulla and the solid cortex still bond well, as the fibrils from both merge into each other and form a continuum, seen in Fig. 15d (except only separation at ventral region in maximum tensile strain in one specimen); the separation within the medulla close to the interface, as mentioned earlier, is very shallow (~one cell thick), which may be from buckling and experimental procedure. This provides desired support from the medulla to the cortex.

## 5. Thoughts for bioinspired designs

The feather shaft shows outstanding structural properties, which can provide useful insights for developing new materials. The sandwich structure featuring a changing shape factor and composed of a complex fibrous solid cortex enclosing a hierarchically porous core produces a structure that is lightweight, strong and stiff, yet reasonably flexible and reliable, properties that have always been the goal for most structural materials. The structure-property knowledge also has value in developing functional materials, e.g. aerospace components including unmanned vehicle materials. Especially fascinating is the topic of autonomous cars, aerial vehicles, e.g. personal aircraft and/or skycars, drones, which are thought to drastically change our life and work in next generations [61]. Lightweight, strong and stiff, renewable materials with ingenious shape designs, resembling the feather shaft, show a great potential for these applications. In addition, the fibrous medulla inside the rachis has hierarchical porosities and can provide useful guidance in developing deformable biomedical materials with recoverable shape.

## 6. Conclusions

The feather shaft represents a naturally refined flight material, whose structure has been oversimplified in the literature. The current work presents a comprehensive study on the flight feather shafts and provides novel findings and quantitative analysis, advancing our knowledge in feather biomechanics and promoting the development of innovative materials. Significant accomplishments from current work are the following:

- The shaft design involves an ingenious combination of a solid cortex, which features a changing shape and differentially aligned fibers, and a medullary core that is also fibrous and has hierarchical porosity; both work synergistically leading to a lightweight, strong and stiff, yet reasonably flexible structure.
- The shaft cortex shows a complex hierarchical structure in multiple length and space scales: the cortex, about 2 mm wide, is composed of keratinized cells about 30–50 μm long and 1 μm thick separated by a 25 nm thick cell membrane complex. Inside the cells are fibers about 3–5 μm, which are composed of macrofibrils measuring about 50–300 nm in diameter surrounded by intermacrofibrillar material observed through TEM. The macrofibrils are further comprised of β-keratin filaments (~3 nm) embedded in electron-dense matrix material. The fibers and fibrils vary in alignment depending on both the specific cortex regions and the position along the shaft length, including axial, circumferential and crossed orientations, verified through nanoindentation.
- The tensile response of cortex strips of dorsal, lateral and ventral regions along the shaft length reveals an increasing Young's modulus in dorsal region towards the distal shaft, but consistently lower modulus in lateral walls throughout rachis, which corroborates the fibrous anisotropic structure. Transverse straight fracture due to rupture of axial fibers and axial splitting are the dominant mechanisms in the dorsal and ventral regions, accompanying crack deflection and fiber bridging, whereas the lateral walls show a zigzag fracture because of crossed-fibers.
- Axial compression reveals that the medulla prevents axial splitting and sudden load drop of the cortex and introduces toughening mechanisms including good interfacial bonding, crack deflection and crack shielding. The cortex in axial compression is accurately modeled by a square tube model; a foam-filled square tube simulating the rachis reveals a synergy between the medulla and cortex. Transverse compression indicates a substantial load-bearing capacity enhancement due to the presence of medulla, e.g. strength increase by a factor of 13.
- Four-point bending tests along the shaft length, analyzed as a composite beam incorporating the medulla, generate decreasing flexural rigidity towards the distal shaft, while the flexural strength in cortex increases. Nevertheless, the specific equivalent flexural modulus and strength (considering each specimen as a homogeneous material normalized by density) increase significantly (by factors of 2 and 3, respectively). Flexural failure occurs by local buckling on the compressive side. Filling the cortex with a foamy medulla prevents destructive axial cracks from propagating and introduces additional toughening mechanisms, e.g. crack deflection, uncracked ligament bridging, fiber bridging and microcracking.

## Acknowledgement

The authors thank Tarah Sullivan for help in obtaining feathers. We appreciate Dr. Wen Yang for help to this research. We also acknowledge Tarah Sullivan, Andrei Pissarenko and Vincent R. Sherman for discussions, and Mason Mackey at National Center for Microscopy and Imaging Research for assistance in TEM. This work is supported by an AFOSR MURI (AFOSR-FA9550-15-1-0009) and a scholarship from China Scholarship Council for Postgraduate Students.

## Appendix A. Supplementary material

Supplementary data associated with this article can be found, in the online version, at http://dx.doi.org/10.1016/j.actbio.2016.11.006.

## References

[1] W.T. Astbury, T.C. Marwick, X-ray interpretation of the molecular structure of feather keratin, Nature 130 (1932) 309–310, http://dx.doi.org/10.1038/130309b0.
[2] R.D.B. Fraser, T.P. MacRae, G.E. Rogers, Keratins: Their Composition, Structure and Biosynthesis, Charles C Thomas, 1972.
[3] R.D.B. Fraser, D.A.D. Parry, The molecular structure of reptilian keratin, Int. J. Biol. Macromol. 19 (1996) 207–211, http://dx.doi.org/10.1016/0141-8130(96)01129-4.
[4] R.D.B. Fraser, D.A.D. Parry, Molecular packing in the feather keratin filament, J. Struct. Biol. 162 (2008) 1–13, http://dx.doi.org/10.1016/j.jsb.2008.01.011.
[5] R.D.B. Fraser, D.A.D. Parry, The structural basis of the filament-matrix texture in the avian/reptilian group of hard β-keratins, J. Struct. Biol. 173 (2011) 391–405, http://dx.doi.org/10.1016/j.jsb.2010.09.020.
[6] B. Wang, W. Yang, J. McKittrick, M.A. Meyers, Keratin: structure, mechanical properties, occurrence in biological organisms, and efforts at bioinspiration, Prog. Mater. Sci. 76 (2016) 229–318, http://dx.doi.org/10.1016/j.pmatsci.2015.06.001.

[7] B.K. Filshie, G.E. Rogers, An electron microscope study of the fine structure of feather keratin, J. Cell Biol. 13 (1962) 1–12, http://dx.doi.org/10.1083/jcb.13.1.1.
[8] G.J. Cameron, T.J. Wess, R.H.C. Bonser, Young's modulus varies with differential orientation of keratin in feathers, J. Struct. Biol. 143 (2003) 118–123, http://dx.doi.org/10.1016/S1047-8477(03)00142-4.
[9] C. Earland, P.R. Blakey, J.G. Stell, Studies on the structure of keratin. IV. The molecular structure of some morphological components of keratins, Biochim. Biophys. Acta 6 (1962) 268–274, http://dx.doi.org/10.1016/0006-3002(62)90564-4.
[10] C. Earland, P.R. Blakey, J.G.P. Stell, Molecular orientation of some keratins, Nature 196 (1962) 1287–1291.
[11] T. Lingham-Soliar, N. Murugan, A new helical crossed-fibre structure of β-Keratin in flight feathers and its biomechanical implications, PLoS ONE 8 (2013) e65849, http://dx.doi.org/10.1371/journal.pone.0065849.
[12] R.H.C. Bonser, P.P. Purslow, The Young's modulus of feather keratin, J. Exp. Biol. 1033 (1995) 1029–1033.
[13] I.M. Weiss, K.P. Schmitt, H.O.K. Kirchner, The peacock's train (*Pavo cristatus* and *Pavo cristatus* mut. alba) I. Structure, mechanics, and chemistry of the tail feather coverts, J. Exp. Zool. Part A Ecol. Genet. Physiol. 313 A (2010) 690–703, http://dx.doi.org/10.1002/jez.671.
[14] S.G. Bodde, M.A. Meyers, J. McKittrick, Correlation of the mechanical and structural properties of cortical rachis keratin of rectrices of the Toco Toucan (*Ramphastos toco*), J. Mech. Behav. Biomed. Mater. 4 (2011) 723–732, http://dx.doi.org/10.1016/j.jmbbm.2011.01.010.
[15] S.P. Timoshenko, J.M. Gere, Theory of Elastic Stability, second ed., McGraw-Hill Book Company Inc., New York, 1961.
[16] L.D. Landau, E.M. Lifshitz, Theory of Elasticity, third ed., Pergamon Press, Oxford, 1986.
[17] G.N. Karam, L.J. Gibson, Elastic buckling of cylindrical shells with elastic cores—I. Analysis, Int. J. Solids Struct. 32 (1995) 1259–1283, http://dx.doi.org/10.1016/0020-7683(94)00147-O.
[18] G.N. Karam, L.J. Gibson, Elastic buckling of cylindrical shells with elastic cores—II. Experiments, Int. J. Solids Struct. 32 (1995) 1285–1306, http://dx.doi.org/10.1016/0020-7683(94)00148-P.
[19] Z.Q. Liu, D. Jiao, M.A. Meyers, Z.F. Zhang, Structure and mechanical properties of naturally occurring lightweight foam-filled cylinder – the peacock's tail coverts shaft and its components, Acta Biomater. 17 (2015) 137–151, http://dx.doi.org/10.1016/j.actbio.2015.01.035.
[20] P.P. Purslow, J.F.V. Vincent, Mechanical properties of primary feathers from the pigeon, J. Exp. Biol. 72 (1978) 251–260.
[21] G.D. Macleod, Mechanical properties of contour feathers, J. Exp. Biol. 87 (1980) 65–71.
[22] S.E. Worcester, The scaling of the size and stiffness of primary flight feathers, J. Zool. 239 (1996) 609–624, http://dx.doi.org/10.1111/j.1469-7998.1996.tb05947.x.
[23] T. Bachmann, J. Emmerlich, W. Baumgartner, J.M. Schneider, H. Wagner, Flexural stiffness of feather shafts: geometry rules over material properties, J. Exp. Biol. 215 (2012) 405–415, http://dx.doi.org/10.1242/jeb.059451.
[24] D.G. Crenshaw, Design and materials of feather shafts: very light, rigid structures, Symp. Soc. Exp. Biol. 34 (1980) 485–486.
[25] W.R. Corning, A.A. Biewener, In vivo strains in pigeon flight feather shafts: implications for structural design, J. Exp. Biol. 201 (Pt 22) (1998) 3057–3065. <http://www.ncbi.nlm.nih.gov/pubmed/9787125>.
[26] B.K. Filshie, G.E. Rogers, The fine structure of α-keratin, J. Mol. Biol. 3 (1961) 784–786.
[27] K. Takahashi, H. Yamamoto, Y. Yokote, M. Hattori, Thermal behavior of fowl feather keratin, Biosci. Biotechnol. Biochem. 68 (2004) 1875–1881, http://dx.doi.org/10.1271/bbb.68.1875.
[28] P.A. Martin, G.D. Bradford, R.M. Gous, A formal method of determining the dietary amino acid requirements of laying-type pullets during their growing period, Br. Poult. Sci. 35 (1994) 709–724, http://dx.doi.org/10.1080/00071669408417737.
[29] W.C. Oliver, G.M. Pharr, An improved technique for determining the hardness and elastic modulus using the load and displacement sensing indentation experiments, J. Mater. Res. 7 (1992) 1564–1583.
[30] W.C. Oliver, G.M. Pharr, Measurement of hardness and elastic modulus by instrumented indentation: advances in understanding and refinements to methodology, J. Mater. Res. 19 (2004) 3–20, http://dx.doi.org/10.1557/jmr.2004.19.1.3.
[31] F.L. Warburton, Determination of the elastic properties of horn keratin, J. Text. Inst. Proc. 39 (1948) 297–308.
[32] L. Farran, A.R. Ennos, M. Starkie, S.J. Eichhorn, Tensile and shear properties of fingernails as a function of a changing humidity environment, J. Biomech. 42 (2009) 1230–1235, http://dx.doi.org/10.1016/j.jbiomech.2009.03.020.
[33] J. Lee, H.J. Kwon, Measurement of stress-strain behaviour of human hair fibres using optical techniques, Int. J. Cosmet. Sci. 35 (2013) 238–243, http://dx.doi.org/10.1111/ics.12031.
[34] B. Wang, M.A. Meyers, Unpublished results, 2016.
[35] G.E. Rogers, Electron microscopy of wool, J. Ultrastruct. Res. 2 (1959) 309–330, http://dx.doi.org/10.1016/S0022-5320(59)80004-6.
[36] P.Y. Chen, J. McKittrick, M.A. Meyers, Biological materials: functional adaptations and bioinspired designs, Prog. Mater. Sci. 57 (2012) 1492–1704, http://dx.doi.org/10.1016/j.pmatsci.2012.03.001.
[37] J.F.V. Vincent, P. Owers, Mechanical design of hedgehog spines and porcupine quills, J. Zool. 210 (1986) 55–75, http://dx.doi.org/10.1111/j.1469-7998.1986.tb03620.x.
[38] L. Gibson, M. Ashby, Cellular Solids: Structure and Properties, second ed., Cambridge University Press, Cambridge, 1997.
[39] W. Yang, J. McKittrick, Separating the influence of the cortex and foam on the mechanical properties of porcupine quills, Acta Biomater. 9 (2013) 9065–9074, http://dx.doi.org/10.1016/j.actbio.2013.07.004.
[40] M.A. Dawson, L.J. Gibson, Biomimetics: extending nature's design of thin-wall shells with cellular cores, Press WIT Trans. Ecol. Environ. 87 (2006) 145–155, http://dx.doi.org/10.2495/DN060141.
[41] R. Weinkamer, P. Fratzl, Mechanical adaptation of biological materials - The examples of bone and wood, Mater. Sci. Eng. C 31 (2011) 1164–1173, http://dx.doi.org/10.1016/j.msec.2010.12.002.
[42] D. Hull, T.W. Clyne, An Introduction to Composite Materials, Press Syndicate of the University of Cambridge, Cambridge, UK, 1996.
[43] M.W. Hyer, Stress Analysis of Fiber-reinforced Composite Materials, McGraw-Hill Companies, Inc., 1998.
[44] C.M. Laurent, C. Palmer, R.P. Boardman, G. Dyke, R.B. Cook, Nanomechanical properties of bird feather rachises: exploring naturally occurring fibre reinforced laminar composites, J. R. Soc. Interface 11 (2014) 20140961.
[45] R.H.C. Bonser, The mechanical performance of meduallary foam from feathers, J. Mater. Sci. Lett. 20 (2001) 941–942.
[46] F. Bleich, Buckling Strength of Metal Structures, McGraw-Hill Book Companies Inc., New York, 1952.
[47] S. Filippov, E. Haseganu, A. Smirnov, Buckling analysis of axially compressed squared elastic tubes with weakly supported edges, Tech. Mech. 20 (2000) 13–20.
[48] G.N. Karam, L.J. Gibson, Biomimicking of animal quills and plant stems: natural cylindrical shells with foam cores, Mater. Sci. Eng. C 2 (1994) 113–132, http://dx.doi.org/10.1016/0928-4931(94)90039-6.
[49] G. Gerard, Introduction to Structural Stability Theory, McGraw-Hill Book Companies, Inc., 1962.
[50] S. Reid, T. Reddy, M.D. Gray, Static and dynamic axial crushing of form-filled sheet metal tubes, Int. J. Mech. Sci. 28 (1986) 295–322.
[51] M. Moradi, S.R. Arwade, Improving buckling response of the square steel tube by using steel foam, Struct. Eng. Mech. 51 (2014) 1017–1036.
[52] P.P. Seide, Compressive buckling of a long simply supported plate on an elastic foundation, J. Aerosp. Sci. 25 (1958) 382–384.
[53] E. Winkler, Die Lehre Von Elasticitaet Und Festigkeit, H. Dominicus, Prague, 1867.
[54] H.G. Allen, Analysis and Design of Structural Sandwich Panels, Pergamon Press, Oxford, 1969.
[55] L.J. Gibson, M.F. Ashby, B.A. Harley, Cellular Materials in Nature and Medicine, Cambridge University Press, Cambridge, UK, 2010.
[56] N. Gupta, P. Ray, Collapse of thin-walled empty and filled square tubes under lateral loading between rigid plates, Int. J. Crashworthiness 3 (1998) 265–285, http://dx.doi.org/10.1533/cras.1998.0075.
[57] R.W. Fitzgerald, Mechanics of Materials, second ed., Addison-Wesley Publishing Company, Inc., 1982.
[58] M.F. Ashby, Materials Selection in Mechanical Design, fourth ed., Elsevier Ltd., Burlington, 2011.
[59] S. Kapila, R. Sachdeva, Mechanical properties and clinical applications of orthodontic wires, Am. J. Orthod. 96 (1989) 100–109.
[60] M.K. Asgharnia, W.A. Brantley, Comparison of bending and tension tests for orthodontic wires, Am. J. Orthod. 89 (1986) 228–236.
[61] P. Moller, Moller skycar, (n.d.). <http://moller.com/>.